Journal of Wind Engineering & Industrial Aerodynamics 213 (2021) 104586

Contents lists available at ScienceDirect

Journal of Wind Engineering & Industrial Aerodynamics

journal homepage: www.elsevier.com/locate/jweia

Aerodynamic shape optimization of rectangular and elliptical double-skin façades to mitigate wind-induced effects on tall buildings

Mohammad Jafari, Alice Alipour *

Department of Civil, Construction and Environmental Engineering, Iowa State University, Ames, IA, 50011, USA

ARTICLE INFO

Keywords:
Aerodynamic shape optimization
Double-skin façade
Design of experiment
Genetic algorithm
Wind-induced load

ABSTRACT

Double-skin façades (DSFs) are high-efficiency systems traditionally used to improve the natural ventilation of buildings for energy-saving purposes and their aesthetic improvement. There are opportunities to enhance their functionality by applying them to improve building aerodynamics. This study aims at developing the preliminar data set that would assist with design of smart morphing facades (also known as Smorphacades). For this purpose the a DSF for rectangular and elliptical tall buildings is studied with the final goal of minimizing the aerodynamic loads on such structures. For this purpose, an integrated framework including numerical modeling and statistical analysis was developed. The design of experiment (DOE) method was applied to produce a sufficient dataset based on computational fluid dynamics (CFD) simulation of two-dimensional (2D) scaled models that were validated with available wind tunnel data. According to the data points recommended by the DOE method, a considerable number of CFD simulations were performed, and the drag coefficients of the building and double-skin façade were separately calculated. A prediction model based on the response surface methodology (RSM) was developed to estimate the drag coefficient for other cases inside the design space. Based on the fitted RSM, the Genetic algorithm was applied to search for the optimized Smorphacade shapes. The results indicated that the integrated smorphacade system could significantly mitigate wind-induced drag forces on the building at all attack angles by modifying wind-induced pressure around the building and weakening vortex shedding by interrupting flow separation and ejecting airflow into a lower-pressure area. This research proves that there are opportunitie to integarte the architectural and energy applications of smart double skin facades with wind-reducing effects as a promising solution for overcoming existing challenges for controlling wind-induced load and response of tall buildings.

1. Introduction

Recent advances in construction techniques along with increasing urbanization have resulted in an increasing trend toward worldwide construction of tall buildings. Such structures are becoming more and more slender and flexible due to an increase in their height and lighter construction material, making them vulnerable to wind-induced vibrations (Hou and Jafari, 2020; Jafari and Alipour, 2020, Jafari et al., 2019, Micheli et al., 2017, 2019, 2020 a, b, and c, 2021). Double-skin façades (DSFs), also known as double façades, ventilated façades, and adaptive skins, have gained growing attention within the architectural engineering community (see Fig. 1). DSFs are commonly implemented to improve indoor climate, save energy, and block sunlight (Pomaranzi et al., 2020). Farrokhzad and Nayebi (2014) showed that the double-skin glass façades could effectively balance energy transfer between indoor and outdoor spaces in high-rise buildings. Stec et al. (2005) placed plants inside double-skin façades, with results indicating that such a combined system could considerably improve the indoor climate and save energy. Moreover, the application of double façades for harvesting energy by the installation of vertical-axis wind turbines between façades (Hassanli et al, 2017, 2018a, 2018b) and building-integrated photovoltaics (BIPVs) has gained much attention (Agathokleous and Kalogirou, 2016; Domjan et al., 2020; Yang et al., 2019). For more information about other applications of such systems, readers are referred to review papers published by Barbosa and Ip (2014) about natural ventilation, by Jiru et al. (2011) on heat transfer aspects, and by Pomponi et al. (2016) related to climate improvement. Both advantages and existing challenges in using these structures can be reviewed in a study by GhaffarianHoseini et al. (2016).

In addition to architectural and energy-saving applications of DSFs,

* Corresponding author.
E-mail address: alipour@iastate.edu (A. Alipour).

https://doi.org/10.1016/j.jweia.2021.104586
Received 14 December 2020; Received in revised form 12 February 2021; Accepted 24 February 2021
Available online 28 April 2021

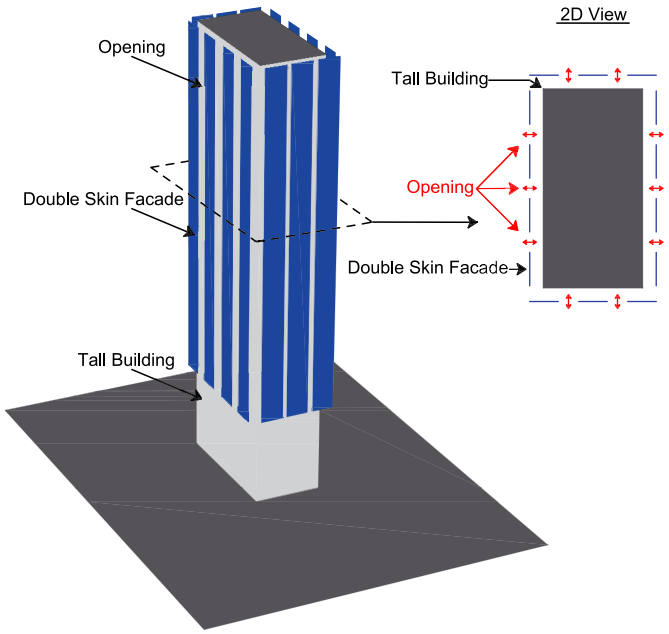

Fig. 1. Double façade with vertical openings attached to a tall building.

conceptual designs have shown that they can efficiently alleviate wind-induced loads acting on a high-rise building (Abdelaziz et al., 2021; Hu et al., 2019; Moon, 2009). There have been a few studies focusing on such effects of double façades on wind response of tall buildings, and most have used wind-tunnel testing on very limited configurations specific to the project at hand. Moon (2009) studied the impact of double-skin façades in reducing wind-induced motion of tall buildings by solving the equations of motion for the primary structure and the façade system and calculate the dynamic response due to wind load. While it was found that a proposed low-stiffness connector for a DSF system can significantly mitigate wind-induced vibration of the building, this system does not necessarily use the DSF to change the structure's aerodynamics and has severe design limitations due to significant motion of the DSF's outer skins. In another study, Moon (2011) installed an extra small mass inside the DSF to provide a damping mechanism similar to a tuned mass damper to overcome vibration issues associated with a previously-designed system. Hu et al. (2019) performed a series of wind-tunnel experiments to assess the effectiveness of attached DSFs with vertical openings in their external skin to alleviate wind-induced pressure on the building's cladding. It was shown that a DSF without such an opening resulted in an increase in mean suction pressure and fluctuating pressure on the leeward face and both sides of the building and led to unsatisfactory performance for the DSF system under extreme wind conditions. Conversely, the pressure was reduced on the leeward face and sides for a DSF with opening(s), so it was concluded that DSFs with openings could effectively improve the wind resistance of claddings in tall buildings if they were designed with vertical openings.

To better understand flow characteristics around a tall building covered by DSFs, Hu et al. (2017) performed a series of boundary-layer wind tunnel experiments. They presented useful information about wind-induced response and pressure distribution around a tall building by monitoring an aeroelastic/flexible building model. Experiments both with and without vertical openings for double façades showed a negligible impact on the building response in the along-wind direction, while in the across-wind direction, it was found that existing openings can notably reduce the wind response compared to a building with a flat side with no façade. In contrast, solid façades with no openings escalated the wind-induced response, and vertical openings in the center produced the most significant effects in terms of reducing fluctuating pressure. Dependency of wind response on façade configuration was also discussed through a cross-correlation analysis along the building height. In another wind-tunnel testing, Da Silva and Gomes (2008) examined DSFs for various multi-story layouts and wind directions while testing for small to large gap depths. Similar to results obtained by Potangaroa and Aynsley (2003), they found that the pressure coefficient within a DSF's gap is always negative for all wind angles. In their façade system, solid with no opening, they found that angles of attack ranging from 0° to 45° significantly affected the pressure distribution pattern. Basaran and Inan (2016) experimentally evaluated pressure loss due to double façades using perforated plates. To this end, they tested different perforated plates and discussed the Reynolds number effect. Gerhardt and Janser (1994) systematically varied building dimensions, façade porosity, and gap width to study their influence on wind loading on a tall building with a double façade. They compared the pressure coefficients for the different cases and validated their wind-tunnel data with field measurement. In another study, the same authors investigated the impact of wind-permeable façades on forces acting on the building (Gerhardt and Kramer, 1983), mainly focusing on the probability distribution of the pressure coefficient and the sensitivity of peak pressure with respect to incoming flow conditions.

Lou et al. (2012) conducted a series of studies on the effects of DSFs on wind-pressure characteristics of tall buildings through numerical modeling and experimental testing (Lou et al., 2012). They captured the pressure distribution for different layouts, incident wind angles, and air corridor width, then applied a zonal approach to model inner-gap pressures over the DSFs. They found that the zonal modeling, while computationally very efficient, produced acceptable results for replacing the CFD modeling and wind-tunnel testing. In other studies (Lou et al, 2008, 2009), they performed wind-tunnel testing to compare the mean and fluctuation pressure distributions of circular and rectangular tall buildings for single- and double-skin façades with arc-shaped and L-shaped configurations and observed no significant difference between single and double façades in terms of wind load acting on the whole structure.

Pomaranzi et al. (2020) tested the aerodynamic performance of a porous double-skin façade through wind-tunnel experiments. Their research was aimed at evaluating the effectiveness of the DSFs on wind-induced pressure on the cladding surface, and it was found that a façade system can reduce both negative and positive peak pressures of the inner glazed façade by up to 40%. They also observed that filtration of the pressure signal positively affected absolute mean values and standard deviations as a result of flow passing through the porous media. Samali et al. (2014) proposed a smart double-façade system for controlling the building's wind-induced load and response that could significantly dissipate wind-induced energy and accordingly damp out the building vibration. They concluded that a smart façade system could reduce the wind-induced response and acceleration of buildings by up to 50% if an efficient system capable of adjusting stiffness was designed. Kwok et al. (2014) tested aerodynamic performance of an innovative façade system with a specific shape for mitigating the wind response, and their wind-tunnel experiments showed that along- and across-wind responses along with the torsional excitation were significantly reduced by DSFs with vertical openings. A study by Montazeri et al. (2013) is one of few studies using CFD techniques to investigate the effectiveness of a staggered semi-open double-skin façade placed in front of the balcony on the enhancement of wind comfort on high-rise buildings. They implemented a three-dimensional (3D) steady simulation using the Reynolds-Averaged Navier Stokes (RANS) model both with and without the façade. Comparing the obtained results with the occupant comfort thresholds by Dutch Wind Nuisance Standard (2006) indicated that local wind speed significantly reduces due to pressure gradient drop across the façade width.

As shown in this review, studies on the performance of DSFs in changing aerodynamic loads on buildings have been limited in their application, considered configurations, and the research methodologies used to prove this concept. Furthermore, no prior study has addressed the effects of important parameters such as wind direction and façade shape

on the aerodynamics of double façades. This calls for more focused research to evaluate the impact of DSFs as wind load altering additions to the building. As such, this paper aims to fill this gap through comprehensive application of CFD and optimization techniques. Increasing the application of CFD techniques to solve problems dealing with fluid mechanics provides an opportunity to try more combinations of DSFs. Compared to wind-tunnel testing, experimentally-validated CFD models can simulate a larger parametric space. Furthermore, CFD allows for capturing continuous data points within the domain of the desired fluid, compared to the limited number of pressure taps commonly used in wind tunnels. The advantages of CFD modeling can overcome the limitations of wind-tunnel experiments and help the research community explore the use of DSFs in decreasing wind-load effects on tall buildings. In this study, a considerable number of CFD simulations suggested by the DOE model were used to implement a robust optimization framework for finding a DSF's optimal shape for providing the lowest drag force on building, double façade, or both.

This paper is organized as follows: Section 2 explains the proposed framework for DSF optimization. Section 3 presents details of the rectangular and elliptical façades used for optimization and numerical modeling. Section 4 describes the numerical modeling, including treatment of boundary conditions and meshing parameters with CFD results. RMS models are presented in Section 5, and a discussion in Section 6 elucidates the optimization results obtained. Concluding remarks are presented in Section 7.

2. Proposed methodology to optimize double façade

To fill the existing knowledge gap on aerodynamic application of DSFs, this study primarily focuses on two popular exterior-façade shapes, rectangular and elliptical double façades. This shape choice is based on a study conducted by Al-Share (2020) on tall buildings of nine metropolitan areas in the United States that found rectangular shapes to be one of the most popular building shapes (66% of all tall buildings). Another reason for choosing the rectangular building shape is the availability of the experimental tests on this shape to support the validation of CFD results. From a cost and ease-of-construction perspective, it would make sense for rectangular buildings to have an exterior façade closest to the main form of the building (hence the choice of rectangular and elliptical secondary façade shapes in this study). Since this study aims to find DSF configurations that would result in lower loads exerted on the building along with limitations of self-excited forces in the building's dynamic response, drag coefficient has been considered the main factor for optimization. The Commonwealth Advisory Aeronautical Council (CAARC) standard tall building (Thompson et al., 2017; Wardlaw and Moss, 1970) was considered as a reference case, and the effects of rectangular and elliptical façades on wind-induced drag load on both the façade and the building were studied. The response surface model (RSM) can provide the approximate values of the output parameters, such as drag coefficient, at given input parameters representing a new geometry. In other words, the RSM can be used as a prediction model to estimate the response variables for new design variables inside the design space. The RSM model was used here for the NSGA-II optimization algorithm to search for a geometry resulting in the lowest drag coefficient. Fig. 2 illustrates the framework proposed in this paper to optimize the DSFs of the tall building considered. The blocks shown in this flowchart will be discussed in the following sections.

The application of the response surface method (RSM) is similar to other machine learning-based prediction models, such as the artificial neural network (ANN), support vector machine (SVM), random forest (RF), decision trees (DT), and regression models. However, the RSM is a simple and powerful tool that is usually applied based on the sampling

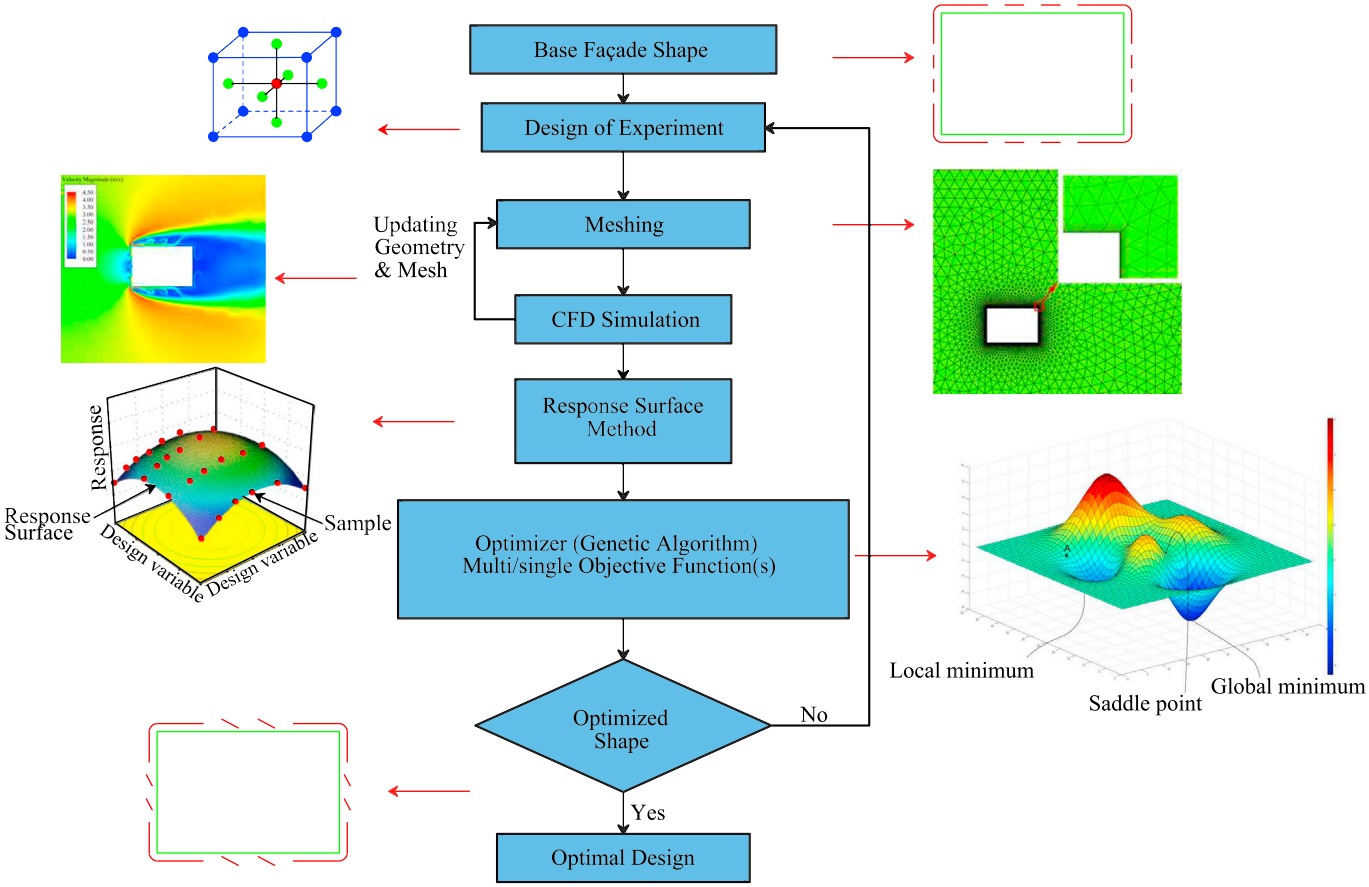

Fig. 2. Flowchart of the proposed procedure for optimizing the characteristics of rectangular and elliptical double facades.

points suggested by the DOE method. The primary advantage of RSM is the small number of training points required to develop a prediction model considering the interaction between variables (Box and Wilson, 1951). The RSM also has some limitations; for example, when the number of variables becomes large, the number of interaction terms increases and results in more complexity, which reduces its applicability (Baş and Boyacı, 2007). Nevertheless, other sophisticated models such as ANN requires a large dataset to provide an accurate prediction, and they typically perform well for a large number of design variables. Eventually, it can be concluded that the RSM usually performs better for cases with limited data points, while other machine learning algorithms have a better performance for big datasets and a large number of design variables.

2.1. Design of experiment (DOE)

In the DOE, a set of measures performed to increase production efficiency, a group of different parameters that affect the outcome of a particular process is analyzed to obtain the best possible values for producing an optimal product. This approach helps in studying experiments with multiple parameters and providing reliable information for determining both significant and ineffective parameters in the desired outcome (Antony, 2014; Manshadi and Aghajanian, 2018). To study the shape effect on the wind-induced load of DSFs attached to a building, it is essential to systematically change the façade shape and run a numerical simulation for each case to capture the aerodynamic forces for design parameters over a wide design space. This approach requires producing a large number of datasets that require updating geometry and mesh for each case, then running the updated computational fluid dynamics (CFD) model. For this purpose, the DOE method was used to reduce the computational cost by providing the required number of sample points. In this study, the Central Composite Design (CCD) sampling method and Latin Hypercube Sampling (LHS) method were employed to determine the required sampling points and their distribution in design space. The CCD sampling method was used to find the sampling points, random points inside the design space used to develop the response surface model. This sampling method has been widely used to fit a second-order model for the response variable. In CCD, there is a central point in the middle of the input design space, with $2k$ axial points on the axes associated with input parameters, and these $2k$ points distributed in the design space are called factorial points. The number of sampling points based on CCD can be calculated using Equation (1).

$$Sampling\ \ points(CCD) = 2^k + 2k + n_c \tag{1}$$

where k is the number of factors or parameters, and n_c is the center point considered to be 1 in this analysis. CCD's main advantage is that variance estimation is the same for points at the same distance from the design center, meaning that all sample points are at the same distance from the design center and have the same variance or deviation. For example, for four input parameters, the total number of sample points based on this approach would be $2^4+2 \times 4 + 1 = 25$. The next method to be applied here is Latin Hypercube Sampling (LHS), an advanced algorithm using the Monte Carlo sampling method. These points are randomly-generated within each of the square grids in the design space, with no two points having the same input parameter value. Since five levels were considered to divide each parameter's design space, the number of sample points for the LHS can be calculated as $2 \times k \times 5 + 1$, where k is the number of parameters. For example, if there were four input parameters, the total number of sample points would be $2 \times 4 \times 5 + 1 = 41$. Table 1 describes how the sampling points were selected in this study for the different cases to be discussed later.

Based on the summation of total sample points listed in the last column of Table 1, the dataset consisting of 967 cases is required for simulation to generate the associated drag coefficients on the building façade. To generate the required large number of simulations identified by DOE, in a manner similar to past studies (Bernardini et al., 2015; Daemei and Eghbali, 2019), two-dimensional (2D) computational fluid dynamics modeling was conducted to assess the aerodynamic performance of DSFs and the buildings. Two-dimensional CFD modeling is much faster and simpler than three-dimensional (3D) modeling because it requires fewer meshes and computational time. On the other hand, some phenomena, such as buoyancy effects, 3D vortices, and fully turbulent flow, could not be captured using 2D modeling. Although the 3D numerical simulations are more realistic and 2D modeling is an idealized version, past studies on aerodynamic optimization of tall buildings have shown that the 2D modeling sufficiently provides accurate results for many cases considering the computational time and cost as key factors (Daemei and Eghbali, 2019; Elshaer et al., 2015). However, the implementation of 2D or 3D simulations mainly depends on the physics of the problem and the project's targets.

Table 1
Sampling points suggested by the DOE.

Cases	Input parameters (k)	Required sample points	Tested attack angles	Total points
Rectangle (step I)	3	2^3+2 × **3** + 1 = 15 (CCD)	10	10 × 15 = 150
Rectangle (step II)	8	2 × **8** × 5 + 1 = 81 (LHS)	7	7 × 81 = 567
Ellipse	4	2^4+2 × **4** + 1 = 25 (CCD)	10	10 × 25 = 250

The DOE requires creating approximately 1000 CFD model simulations. The high computational cost associated with generating these CFD models derived the decision to conduct 2D CFD models for this study. Furthermore, for the purpose of aerodynamic modification, double façades are normally placed at upper levels. As such the along-height aspect ratio of a tall building is large enough to ignore three-dimensional effects such as the horseshoe vortex that mainly occur near the ground (Baker, 1979; Peterka et al., 1985; Sattar et al., 2018; Song and He, 1993). It is expected that with the promising results presented in this paper from 2D CFD modeling, the high-fidelity 3D CFD simulations combined with wind-tunnel experiments can be developed to more precisely elaborate the flow characteristics around selected double-façade designs for further development and implementation.

2.2. Optimization algorithm

In this study, the Genetic Algorithm (GA) was used to determine the global minimum in the optimization problem for minimizing the error between the fitted surface and sample point values (Arora, 2004a). Amongst various methods, the genetic algorithm has proven to be robust in solving such multi-objective optimization problems due to its power to accurately provide a uniform, efficient, and well-distributed Pareto frontier (Manshadi and Aghajanian, 2018; Parashar and Bloebaum, 2006). Simple implementation and high likelihood of approaching the global minimum are other advantages of this gradient-free optimization method (Kenway and Martins, 2016). The GA method is an excellent choice for cases with a small number of design variables like in this study. After running the simulations for sample points, as explained in Section 2.1, to identify the drag coefficients of the building and façade as the objective functions, the response surface model (RSM) was fitted to predict the other unknown drag coefficients. Eventually, this requires solving a multi-objective problem, generally mathematically-defined by Equation (2), and determine the optimal shape corresponding to the minimum drag force.

$$\mathrm{Min}(f_1(x), f_2(x), \ \ldots, f_k(x)) \quad subject\ to\ x \in X \tag{2}$$

where k is the number of objectives, two in this study, and X is the feasible set of decision vectors. In a multi-objective or Pareto optimiza-

tion problem, there are a couple of objective functions subjected to equality and/or inequality constraints, and the goal is to find the values of design variables leading to the lowest cost for these objective functions. In most cases, it can be seen that these objective functions contradict each other in such a way that increasing one results in decreasing the other(s). In such cases, the optimization algorithm results in the Pareto front curve that helps choose the optimal point(s) that satisfy the subjective preferences. The NSGA-II method proposed by Deb et al. (2002) is a modified version of the Non-dominated Sorting Genetic algorithm that has been widely employed for engineering applications in a variety of applications because of its low computational requirements, its elitist approach, and its parameterless sharing approach (Deb et al., 2000). Finding optimal design variables giving the minimum or maximum objective functions that are drag coefficients first requires a prediction model that can estimate the objective functions inside the design space. For this purpose, the response surface model was first fitted with the data obtained from CFD, after which the NSGA-II algorithm was used to determine the optimal DSF shape with the lowest drag coefficients both for the building and the façade.

The optimization problem can be divided into a single or a multi-objective optimization algorithm depending on the number of objective functions. For this purpose, to find the optimal geometry, single (minimizing only the building's drag coefficient) and multi-objective (minimizing the drag coefficients of both building and façade) optimization problems were solved for each wind direction. The statistical analysis indicates that the façade geometry and wind direction nonlinearly influence the wind load, leading to more complexity in finding the best design for the double façade. Because of this, this study justifies developing smart façades with the capability of adjusting their shape according to wind direction as an innovative solution for aerodynamic modification of the building to mitigate wind-induced loads and responses on tall buildings.

3. Geometric description of double façades

This study used a series of two-dimensional (2D) numerical simulations to investigate the influence of rectangular and elliptical double façades on wind-induced drag forces exerted on the CAARC building, with the exterior façade (representing the Smorphacade) and building model with $B/D = 1.5$ scaled down to 1:100 for numerical modeling. A schematic view of the building's cross-section covered by rectangular and elliptical facade is displayed in Fig. 3. To design the openings (see Fig. 2), the façade on each side was divided into ten segments, and for each side, while the corners are fixed, four segments are extendable/variable, and three segments are designed as openings (see Fig. 3). As shown in Fig. 3-top, the façade thickness is 1 mm (=10 cm at full-scale).

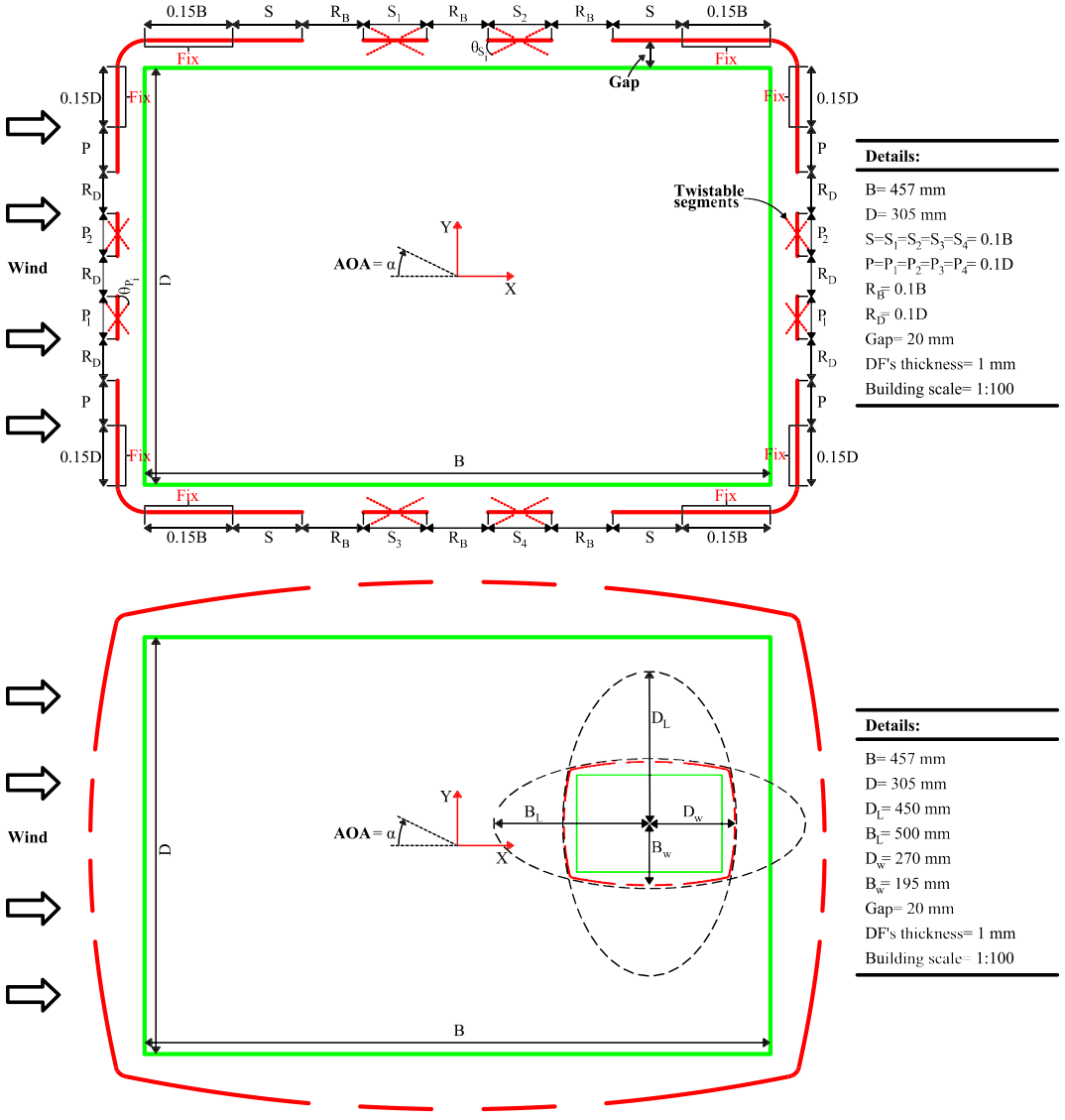

Fig. 3. Schematic view and dimensions of the building's cross-section with (top) rectangular and (bottom) elliptical double façades.

The gap between the double façade and the building is 20 mm (= 2 m at full-scale), and the shorter side (D) and longer side (B) dimensions are 305 and 457 mm (=30.5 m and 45.7 m at full scale), respectively.

After preliminary analysis, three openings were designed for each side, with the focus on finding the optimal number and location. On the windward and leeward faces of the building, there were three openings of length R_D, initially taken as 0.1D. There were four extendable/variable façade segments on the windward side (P,P,P_1,P_2) and four segments on the leeward side (P,P,P_3,P_4), all are initially equal to R_D. Similarly, there were three openings on each side of the building of length R_B, initially 0.1 B. It should be noted that the optimization of the rectangular façade was conducted in two steps. First, three parameters were optimized, including gap, top and bottom segments (S and S_i), and front and back segments ($P$and P_i) for different angles of attack (α). Since the drag coefficients of the CAARC building and the double façade were captured while changing the design variables, there are three design variables: S, P, and gap, in this step. The second optimization step is twisting the angle of the two middle façades (S_i and P_i where $i = 1, 2, 3, 4$) to determine the optimal twist angle resulting in the lowest drag coefficient for each attack angle (α). In Fig. 3-top, the dotted lines indicate that these segments are twistable, resulting in eight design variables in general. Fig. 3-bottom shows how the elliptical façade was fitted with two other ellipses to adjust its shape. Similar to the rectangular façade, three openings were considered for each side, and the four design variables used to change the ellipse shape are B_L,B_W,D_L,andD_W. It should be noted that the opening lengths are fixed in elliptical DSF and are equal to the optimal opening length found for the first-step rectangular façade optimization.

4. Numerical modeling

In CFD analysis, ANSYS Fluent 19.2 software was used for two-dimensional (2D) numerical modeling, using the boundary conditions and dimensions shown in Fig. 4. To model the moving incompressible airflow inside the computational domain, tRANS equations were solved using the $k-\omega$Shear Stress Transport (SST) turbulence model. The second-order upwind was used for spatial discretization, and the SIMPLE algorithm was used for coupling pressure and velocity terms. The minimum acceptable residual was set at 10^{-5} for all equations. As shown in Fig. 4, the inlet boundary condition was set as the velocity inlet, and the inlet turbulence intensity was 10%. The symmetry boundary condition was assigned to the sidewalls to minimize wall effects. The pressure outlet was selected for the output, and the no-slip wall condition was chosen for the building and double façade. The airflow was used as the fluid domain for modeling, and the density (ρ) and dynamic viscosity (μ) were 1.225 kg m^{-3} and 1.7894 $\times$ 10^{-5} kg/m.s, respectively.

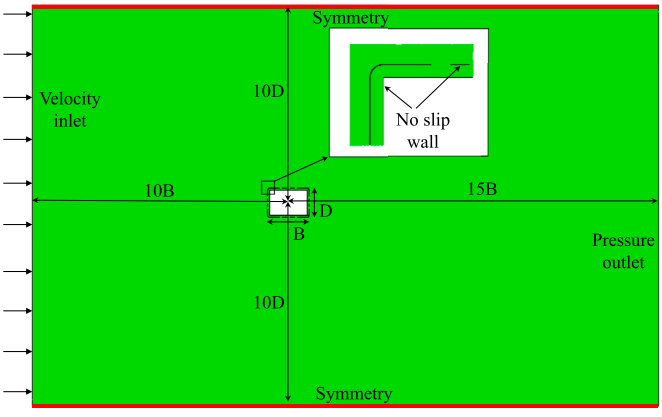

Fig. 4. Boundary conditions and dimensions of the computational domain for numerical simulations.

4.1. Meshing

To increase accuracy and reduce processing time, it is crucial to generate a high-quality mesh for numerical analysis. There are two primary techniques for checking mesh quality inside the computational domain. The first, examining mesh number dependency, is grid independency or grid sensitivity checking. For this purpose, mesh independency was checked by monitoring the drag coefficient for a bare building with no façade. Six different grids, ranging from 30,000 to 150,000 nodes with approximate increments of 24,000, were generated inside the computational domain, and the drag coefficients of objects were monitored. Since it was observed that the variation of drag coefficient after the fourth grid point was negligible, the case with 93,189 unstructured meshes was selected as sufficient for achieving robust simulations. The second approach for assuring mesh quality over the wall surfaces is to track the Y-plus and ensure that it meets the required value suggested for a specific turbulence model (Kalitzin et al., 2005). To ensure that the Y-plus does not exceed 1.0, a ten-layer-boundary-layer mesh with the growth rate 1.2 was generated for both the building and the double façade, and the first cell height, the perpendicular distance from the wall to the first layer, was set to 0.01 mm. The hybrid mesh, including boundary layer and unstructured grids generated for a building and rectangular façade, is illustrated in Fig. 5.

4.2. CFD validation

To ensure representative CFD model results, in addition to the extensive mesh sensitivity analysis and Y-plus check, the numerical results were validated with experimental data produced by Fangwei and Sarkar (2018) for a similar CAARC building model. To obtain the static mean load coefficients, Fangwei and Sarkar (2018) tested a section model (1:400 scale) of a tall building of rectangular cross-section in the aerodynamic test section (uniform flow) of a closed-circuit wind tunnel. The section model dimensions were: length L = 1.140 m, width B = 0.114 m, depth D = 0.076 m, and width-to-depth ratio (B/D) of 1.5, values similar to those of this study. Two 64-channel pressure transducers were employed to measure surface pressures on the model, with 36 pressure taps at three locations distributed around its cross-section. Surface pressures were integrated to obtain the mean aerodynamic loads on the model, and the model was tested at various attack angles (α) measured ranging from 0° to 90°. They attached two endplates at the end of the model to generate two-dimensional (2D) flow around the section model and minimize edge effects. For more details on the experiment setup, refer to (Hou and Sarkar, 2018). For the validation part of the 2D modeling, the drag coefficient of a bare building similar to the wind-tunnel model with $B/D = 1.5$ was compared to experimental data at the same Reynolds number, 6.24 $\times$ 10^4. Drag coefficient results for two angles of attack (AOA), 0° and 90°, at a Reynolds number of 6.24 $\times$ 10^4, are compared in Table 2. The comparison proves the good match between the CFD results and wind-tunnel data. The difference that exists may originate from different sources, including but not limited to the numerical error, the turbulence model used for CFD, and the steady-state simulation used in the current modeling. However, the experimental data may also have errors originating from instrument, measurement, or data analysis.

4.3. CFD models and impact of DSFs on flow around the building

Fig. 6 shows the velocity contour around a bare building without any DSFs. For all simulations, including double façades, the wind speed was fixed at 3 m/s, associated with a Reynolds number ($Re = \rho UD/\mu$) of 6.24 $\times$ 10^4. As shown in Fig. 6, the wake region for the building placed at α = 90° is much bigger than for α = 0° because the frontal area of the building located at α = 90° is wider in the across-wind direction, resulting in a larger suction area and drag force for this case compared to other angles of attack. This larger wake area representing the suction

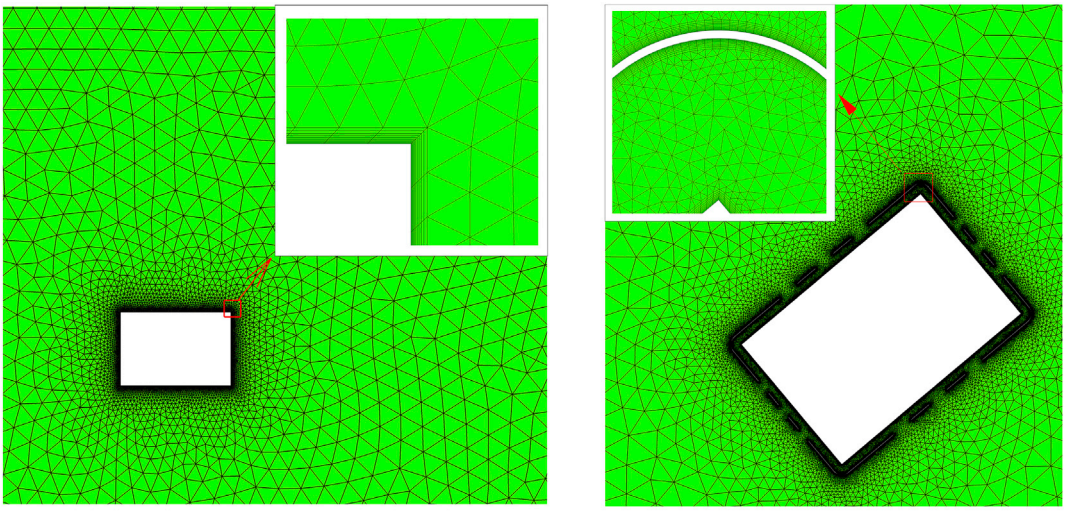

Fig. 5. Mesh generation and boundary layer grid on surfaces of the tall building and façade.

Table 2
Comparison of numerical results and experimental data for a CAARC building with $B/D = 1.5$.

AOA (α)	CFD($k-\omega$,SST)	Experiment (Hou and Sarkar, 2018)	Error (%)
0°	1.270	1.211	4.8
90°	2.828	2.926	3.3

force produces the largest drag force for cases in which the mean wind approaches the building with an attack angle near 90°.

Fig. 7 compares the velocity contours plotted in the range 0–4.5 m/s for a building with rectangular and elliptical DSFs at $\alpha = 0°$, 50°, and 90°. It can be seen that the façades with vertical openings acting as porous media around a building can efficiently distribute the incoming flow into both sides and the wake/behind area. This shows that the double façades transfer more airflow into the wake area when located at $\alpha = 90°$ because the fluid needs to pass over a shorter path in this position, so more flow remains to be ejected from the leeward openings. Since the flow jets toward the suction area can potentially mitigate the wind-induced load due to positive pressure and breaking the vortex shedding that reduces the vortex-induced force's strength, this vortex-shedding interruption leads to a significant reduction in the building's vortex-induced response. Fig. 7 also shows that the maximum velocity inside the gap occurs at the front corners. Comparing the results obtained for rectangular and elliptical façades shows a high degree of similarity for flow behavior passing the façades, while flow separations on the longer sides of the building show up for elliptical DSF. Although designing an oval shape for a double façade provides a more streamlined body that minimizes the separation region more than the rectangular one, especially at zero AOA, it notably influences the aerodynamics of the façade by changing flow characteristics depending on the ellipse dimensions.

5. Response surface model

In statistics, the response surface method (RMS) defines the relationship between explanatory/design variables and response or target parameters. This method, employing sequences of designed experiments to determine an optimal response, was introduced in the early 1950s by

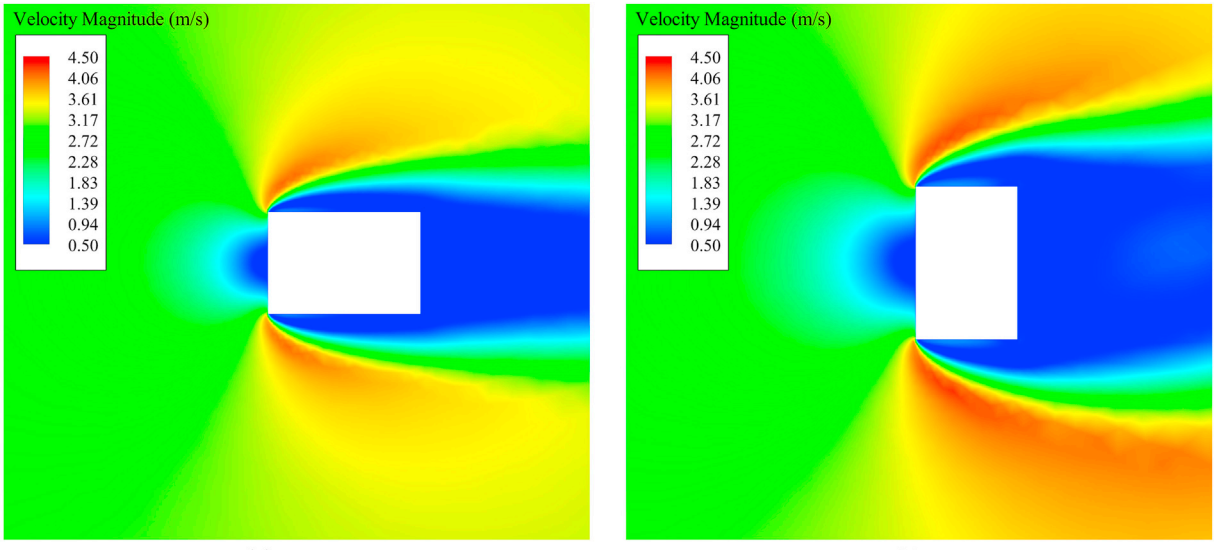

Fig. 6. Velocity contours around a CAARC building plotted for different angles of attack.

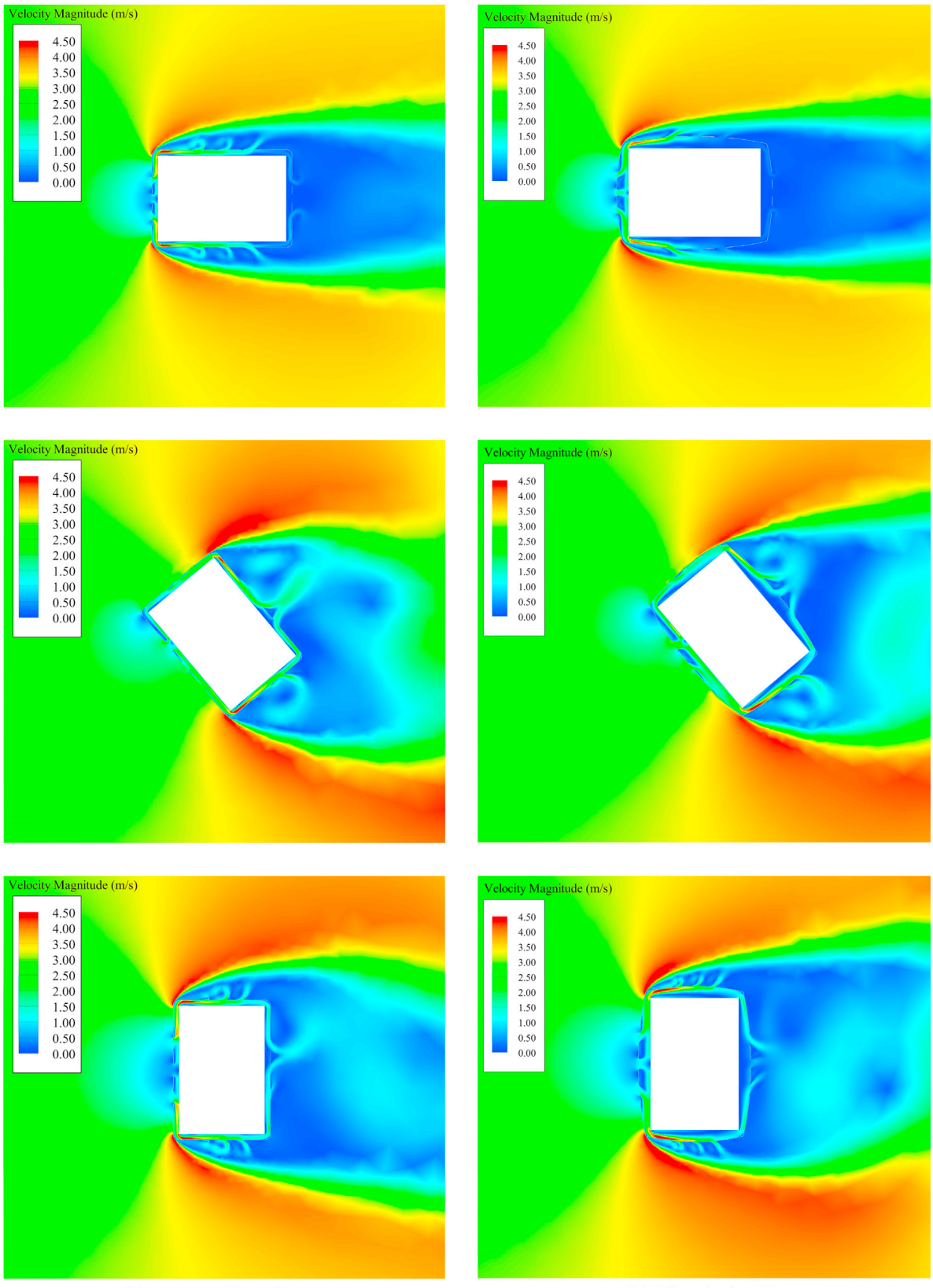

Fig. 7. Velocity contours around a bare building with rectangular and elliptical façades plotted for different angles of attack.

Box and Wilson (1951). The RMS, a useful mathematical tool for approximating stochastic models, has other applications such as optimization, design development, and new product formulation (Myers et al., 2016). The RMS, when applied to construct a meta-model, uses linear or quadratic functions whose coefficients are found by minimizing the error between actual values and estimations. The RMS model is usually applied to data collected from the DOE to construct a precise approximation tool for predicting new experiments or developing optimization algorithms. To this end, the following steps for RMS implementation are required: (a) Sample-point selection using the DOE method to produce response surfaces, (b) Response-surface generation based on function values at experimental sampling points (Arora, 2004b).

In this section, a dataset of aerodynamic coefficients was collected from RANS modeling at particular design variables suggested by the DOE. A response-surface model (RSM) was then fitted with design and response variables to use the fitted prediction model for the optimization algorithm described in the next section. For this purpose, it is essential to make sure that the fitted RSM accurately predicts response variables that are here the drag coefficients of the building and the DSF. Fig. 8, as a sample case, compares the normalized values of the CFD-identified drag coefficient and the RSM-predicted drag coefficient to illustrate how well the prediction model performs.

6. Optimization to find optimal configuration of façades

The optimization procedure can be performed using the RSM model developed here to predict any data points within the defined design space of 967 simulations. The objective functions here are the drag coefficients acting on the CAARC building and the façade, as described in Equations (3) and (4).

$$C_D^B = F_{Drag}^{Building} \Big/ 0.5\rho U^2\sqrt{BD} \tag{3}$$

$$C_D^F = F_{Drag}^{Facade} \Big/ 0.5\rho U^2\sqrt{BD} \tag{4}$$

where $B$is the building length, D is the building width, U is the upstream wind speed, and$F_{Drag}^{Building}$ and F_{Drag}^{Facade} are the respective drag forces acting on the building and double façade. Since changing the façade geometry to minimize the drag force on the building often leads to the force increase on the DSF, these two objectives conflict with one another during the optimization process, with the result that varying the design variables inside the design space results in a Pareto front for the present multi-objective optimization problem. For example, a sample Pareto front for a rectangular façade at $\alpha = 0°$ is shown in Fig. 9, and as can be seen, the response variables values inversely change if either is increased. The optimization results for rectangular and elliptical façades are individually explained in Sections 6.1 and 6.2.

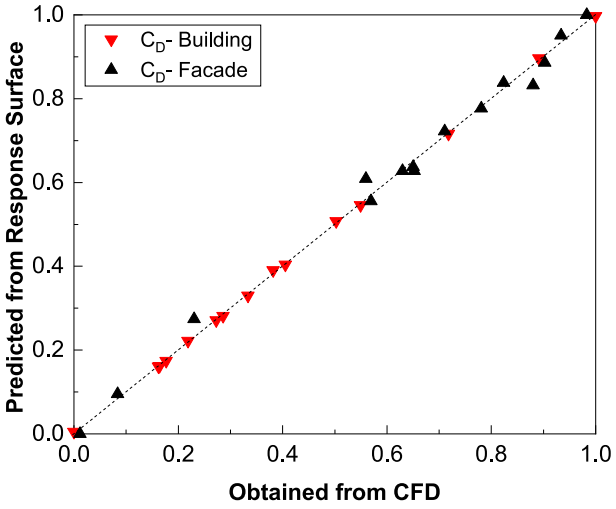

Fig. 8. Normalized values from CFD and predicted by the RSM model.

6.1. Rectangular double façade

6.1.1. Optimization step I

The rectangular-façade optimization was carried out in two steps. First, three design variables, the longer-side ($S\&S_i$) façade segment, the shorter-side ($P\&P_i$) façade segment, and the gap between façade and building were considered (see Fig. 3). It should be noted that in this step, the P is equal to P_i, and the S is equal to S_i. The variables (S/S_i and P/P_i) indirectly adjust the length of openings. As mentioned earlier, according to the DOE and the CCD sampling method, since the simulations for 15 sample points at desired angles of attack must be run to investigate the impact of wind direction, 150 (10 [angle] × 15 [sample]) CFD simulations are required for fitting the RSM model. After running the numerical simulations for these sampling points, the drag coefficients ($C_D^B$and C_D^F) were calculated for different attack angles ranging from 0° to 90° at 10° intervals, and the sampling points and the CFD-obtained drag coefficients are listed in Table 3. The single and multi-objective optimization problems were solved based on the dataset presented in Table 3.

Since the actual wind direction for tall buildings varies, it is crucial to understand a given structure's aerodynamic behavior at various attack angles, and fitting the response surface provides us with an opportunity to visualize the sensitivity of response variables (C_D^B and C_D^F) against design variables (S, P, and Gap). Fig. 10 illustrates this relative sensitivity for different attack angles (the others are presented in Appendix-Figure A1). These bar plots prove that the influence of design variables on drag force acting on either DSF or building significantly depends on wind direction, and this dependency emphasizes the necessity of designing smart double façades for future tall buildings able to adjust their shapes according to the wind direction, similar to those described in a recent study (Attia et al., 2018). Although there is no evident trend for the impact of these design variables, it can be generally seen that the P variables or shorter-side openings are the most influential parameter at small α, while S variables or longer-side openings are most effective at larger α values.

A correlation map is another informative graph illustrating how design and response parameters are correlated at each wind direction. Fig. 11 displays a correlation map between variables for different attack angles (the others are presented in Appendix-Figure A2). In this figure,

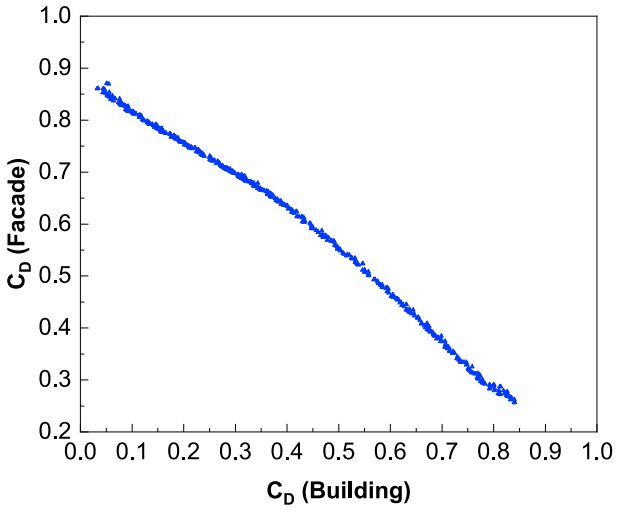

Fig. 9. Sample Pareto front to find the minimum drag coefficient for building and façade at $\alpha = 0°$.

Table 3
Sample points and CFD drag coefficients of the rectangular DSF.

	Design variable (mm)			Angle of attack α°, $\frac{C_D Building}{C_D Facade}$									
	$S\&S_i$	$P\&P_i$	Gap	0°	10°	20°	30°	40°	50°	60°	70°	80°	90°
1	45.7	30.5	20	0.73	0.74	1.21	1.53	1.53	1.78	1.88	1.38	1.20	1.59
				0.35	0.31	0.33	0.38	0.38	0.46	0.50	0.38	0.54	0.56
2	30	30	20	0.76	0.72	1.22	1.53	1.53	2.23	1.86	1.85	1.40	1.75
				0.28	0.29	0.33	0.31	0.31	0.33	0.33	0.45	0.38	0.54
3	60	30	20	0.73	0.79	1.16	1.33	1.33	1.63	1.67	1.63	1.40	1.37
				0.36	0.29	0.35	0.52	0.52	0.71	0.74	0.49	0.81	0.57
4	45	15	20	0.83	0.95	1.13	1.65	1.65	1.83	1.80	1.53	1.70	1.62
				0.20	0.14	0.30	0.31	0.31	0.35	0.35	0.20	0.45	0.43
5	45	45	20	0.33	0.29	1.20	1.14	1.14	1.56	1.91	1.23	1.28	1.24
				0.80	0.76	0.38	0.82	0.82	0.65	0.68	0.68	0.54	0.86
6	45	30	10	0.88	0.80	1.27	1.74	1.74	2.29	2.13	1.78	1.59	1.52
				0.27	0.23	0.29	0.26	0.26	0.36	0.28	0.33	0.50	0.51
7	45	30	30	0.67	0.77	1.18	1.27	1.27	1.55	1.61	1.85	1.15	1.51
				0.31	0.29	0.37	0.63	0.63	0.71	0.65	0.37	0.53	0.56
8	32.80	17.80	11.86	0.93	0.90	1.28	1.83	1.83	2.17	2.11	2.07	1.57	1.69
				0.19	0.16	0.26	0.13	0.13	0.21	0.20	0.34	0.38	0.40
9	57.19	17.80	11.86	0.90	0.87	1.17	1.63	1.63	1.90	2.07	2.07	1.42	1.57
				0.23	0.17	0.28	0.27	0.27	0.33	0.32	0.30	0.60	0.37
10	32.80	42.19	11.86	0.71	0.68	1.20	1.46	1.46	2.12	2.04	1.45	1.44	1.53
				0.43	0.41	0.31	0.38	0.38	0.34	0.35	0.56	0.47	0.65
11	57.19	42.19	11.86	0.68	0.63	1.15	1.43	1.43	1.78	2.02	1.17	1.56	1.03
				0.47	0.42	0.33	0.51	0.51	0.52	0.53	0.74	0.69	0.85
12	32.80	17.80	28.13	0.87	0.98	1.12	1.52	1.52	1.78	1.82	1.41	1.54	1.77
				0.07	0.11	0.32	0.36	0.36	0.41	0.41	0.33	0.27	0.48
13	57.19	17.80	28.13	0.81	0.88	1.24	1.27	1.27	1.56	1.49	1.56	1.00	1.65
				0.19	0.14	0.31	0.53	0.53	0.73	0.73	0.35	0.73	0.39
14	32.80	42.19	28.13	0.47	0.42	1.11	1.10	1.10	1.59	1.56	1.71	1.60	1.65
				0.59	0.63	0.42	0.86	0.86	0.67	0.64	0.60	0.34	0.67
15	57.19	42.19	28.13	0.38	0.42	1.09	0.87	0.87	1.37	1.20	1.35	1.00	1.25
				0.72	0.65	0.39	1.09	1.09	1.07	1.07	0.80	0.79	0.92

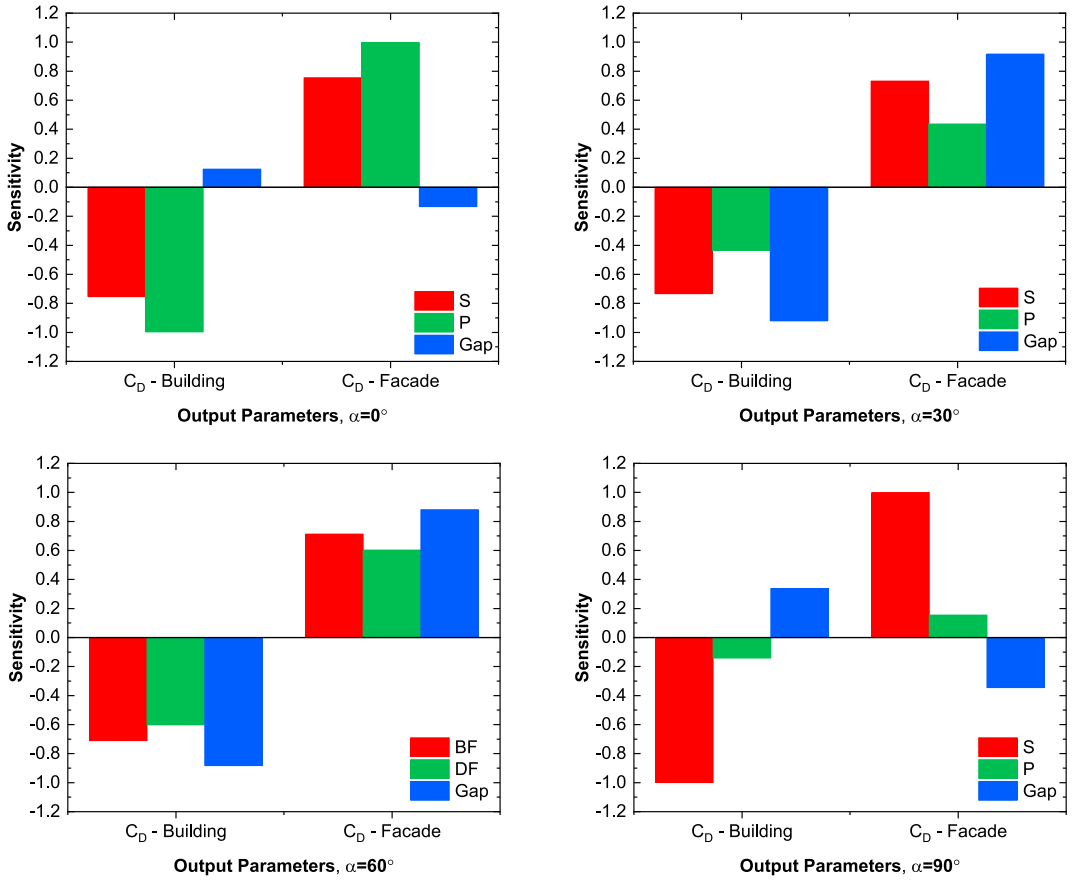

Fig. 10. Relative sensitivity of the drag coefficient of building and rectangular façade against design variables *S*, *P*, and Gap.

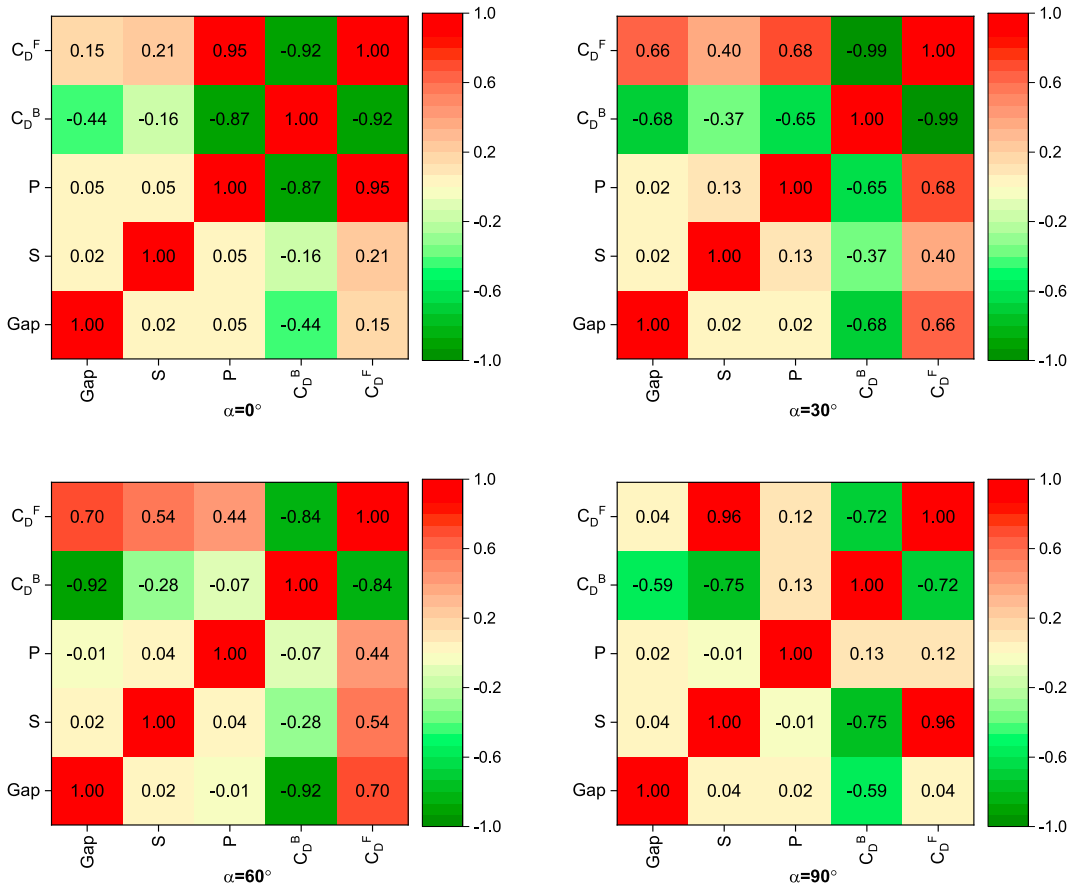

Fig. 11. Correlation map for design and response variables.

C_D^B and C_D^F represent respective drag coefficients of building and rectangular DSF. The red color signifies a positive correlation, while the green color represents a negative correlation between the two quantities. The graphs exhibit no evident predictable pattern while indicating the high dependency of wind direction on drag force and random effects, reflecting the presence of nonlinear terms between design and target variables. Since this random correlation makes the design of double façades even more complicated if the purpose is to tailor it for an aerodynamic modification for mitigating wind-induced load and response, the best solution is to come up with a new design system with the capability for repositioning according to feedback received from sensors monitoring the building response.

It is first crucial to capture the aerodynamic behavior of a building with a rectangular DSF as a base design to allow performance judgment of the optimal configuration. For this purpose, a series of numerical simulations were performed to compute the $C_D$of building with rectangular DSF at various wind directions. Fig. 12 demonstrates the CFD results of a rectangular DSF attached to a CAARC building along with the results of a bare building with no façade. Compared to a bare building, it can be seen that the double façades with openings mostly reduce the overall load at low ($\alpha \approx 0°$) and high ($\alpha \approx 90°$) attack angles. The highest drag force shows up close to $\alpha \approx 45°$ because of having a larger suction area in the wake region at this position (see Fig. 7). However, the DSF system can excellently transfer the load from the building to the façade surface, which is easier to control from the structural design perspective.

Optimally transferring a load from a building to a façade depends on the project goal. Fig. 13a illustrates the optimization and bare building results, in which the only cost function is the building's drag coefficient. While it can be seen that the drag coefficient of the building can be significantly reduced by transferring the load to the DSF structure if the aim is only to minimize the drag force on the building, the total force

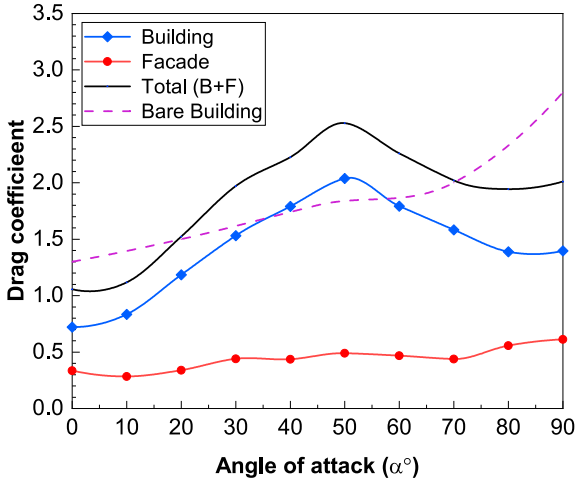

Fig. 12. Drag coefficients of a CAARC building with a rectangular façade (base/initial design).

does not notably change even after the optimization process. To explore the effect of the objective function on load reduction in more depth, a multi-objective optimization problem, minimizing the drag coefficients on both building and façade, was applied to determine the design variables resulting in the lowest force at each angle of attack. The optimization results shown in Fig. 13b prove that the wind force can be significantly reduced with a proper DSF configuration at each wind direction. Although the optimal shape was found for each wind direction, it is beneficial to determine an overall shape for non-adjustable façades offering the best aerodynamic performance for all wind directions. A

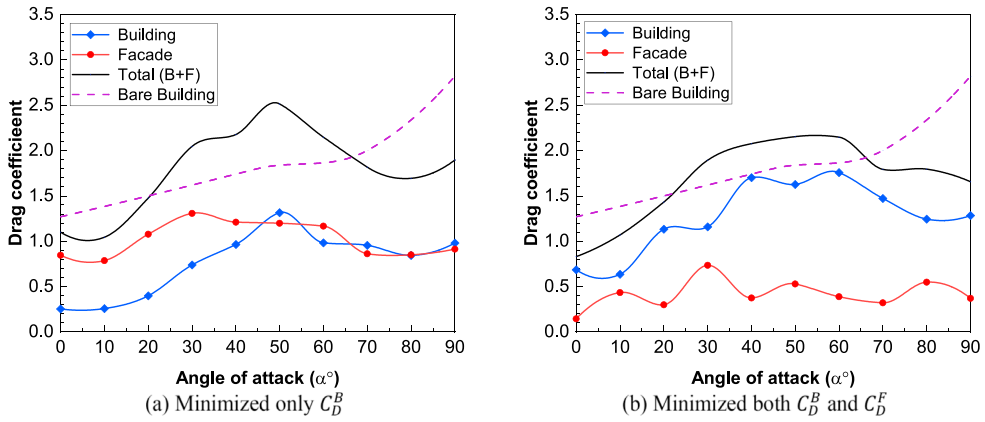

Fig. 13. Single and multi-objective optimization results after minimizing the drag force for the rectangular façade (Step I).

comparison of total force that includes the building and façade loads indicates that a lower total force can be reached based on the multi-objective optimization problem. Although a double façade system may not be specifically classified as an aerodynamic modification approach, this system can be modified to improve a tall building's aerodynamic performance, with a double façade used for other purposes than load reduction. From a design perspective, it is beneficial to transfer the overall wind load acting on a bare building to specific locations to increase the tall building's structural strength only in those areas. Double façades can properly distribute the wind-induced load, and even adaptive façades can perform better at different wind speeds and attack angles.

Finally, to find a shape with the best performance in all AOAs, another optimization was conducted based on the ten optimal designs plotted in Fig. 14b. In Table 4, the optimal design variables for façade length and gap are compared with the base design, the initial configuration of the double façade before any optimization. For all angles of attack, the simulations with optimal geometry described in Table 4 were carried out to evaluate the aerodynamic performance of the optimal façade configuration. To this end, the RSM model already fitted with the dataset was used to estimate the drag coefficients for the simulated geometry. The drag coefficients identified by CFD simulation and RSM estimation are compared for various attack angles in Fig. 15, and it can be seen that these two approaches lead to very similar results that again confirm the accuracy of the fitted RSM model. As shown in Fig. 15, the drag force on a building can be significantly reduced through an optimization process. Although the results presented in this section indicate that non-optimized double façades alleviate the building's drag force, it can be seen that even

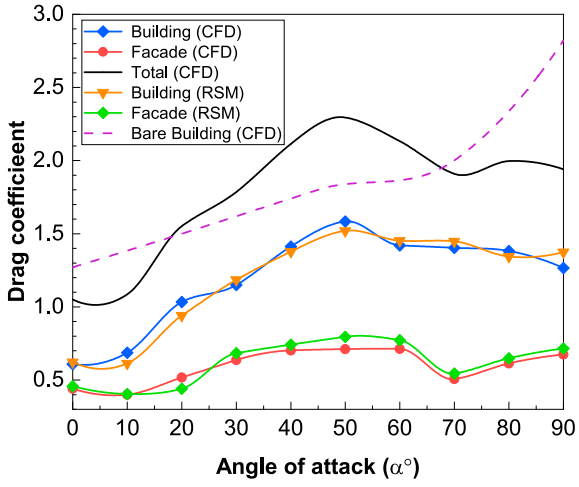

Fig. 14. CFD results and predicted values of the fitted RSM using the optimized shape reported in Table 4.

Table 4
Comparison of optimized design variables and base design (initial design with rectangular DSF).

	$S = S_i$ (mm)	$P = P_i$ (mm)	Gap (mm)
Base design	45.7	30.5	20
Optimal design	50.495	35.033	26.222

the drag force can be reduced more through modification of the façade shape. Comparison of Figs. 13 and 15 proves that the C_D^Bcan be reduced by up to 25% through the optimization process for the three design variables used in Step I. This reduction of wind-induced forces can result in a more economical design for the tall-building structure.

6.1.2. *Optimization step II*

While the proposed optimization approach presented in Step I has resulted in the design of a passive DSF with a geometric configuration that results in the lowest aerodynamic loads exerted on the building and façade, the wind direction changes over time and affects aerodynamic loads applied to tall buildings. To account for such loading variability, this section also considers the performance of the middle DSFs with the capability of twisting out-of-plane (see Fig. 3). These twistable façades on the longer and shorter sides were defined as S_i and P_i in Fig. 3. It has been assumed that these components independently twist from −30° (counter-clockwise) to +30° (clock-wise) to adjust their positions according to the wind direction. The respective twist angles for longer and shorter sides are designated as θ_{S_i} and θ_{P_i}, resulting in eight twistable segments (two at each side). Since the number of design variables in this step is sufficiently large, instead of CCD, the Latin Hypercube Sampling (LHS) method was applied to generate the near-random sample points. According to the LHS method, 81 sample points inside the design space are required to be tested for design variables θ_{S_i} and θ_{P_i} , $i = 1, 2, 3, 4$. These 81 sample points are reported in Table A1 (see Appendix). To study wind-direction effects, seven angles of attack α : 0°, 15°, 30°, 45°, 60°, 75°, and 90°, were considered, resulting in 567 (7 [angle] × 81 [sample]) CFD simulations (as mentioned earlier) for fitting an RSM model. Finally, a large dataset was collected after changing the geometry, updating the mesh, and running the CFD solver for each sample point (SP) described in Table A1 (see Appendix). The numerical results obtained are summarized for each AOA in Table A2 (see Appendix). The data provided in this table enabled us to fit an accurate RSM model for predicting drag coefficients of new points. It should be noted that the optimized values found in the first step were utilized for designing the initial façade in this step.

Similar to the first optimization step, a sensitivity graph and a correlation map, two powerful statistical tools, are plotted to visualize the effects of design variables on output parameters. These two graphs are illustrated for three angles of attack in Fig. 15, with the others presented

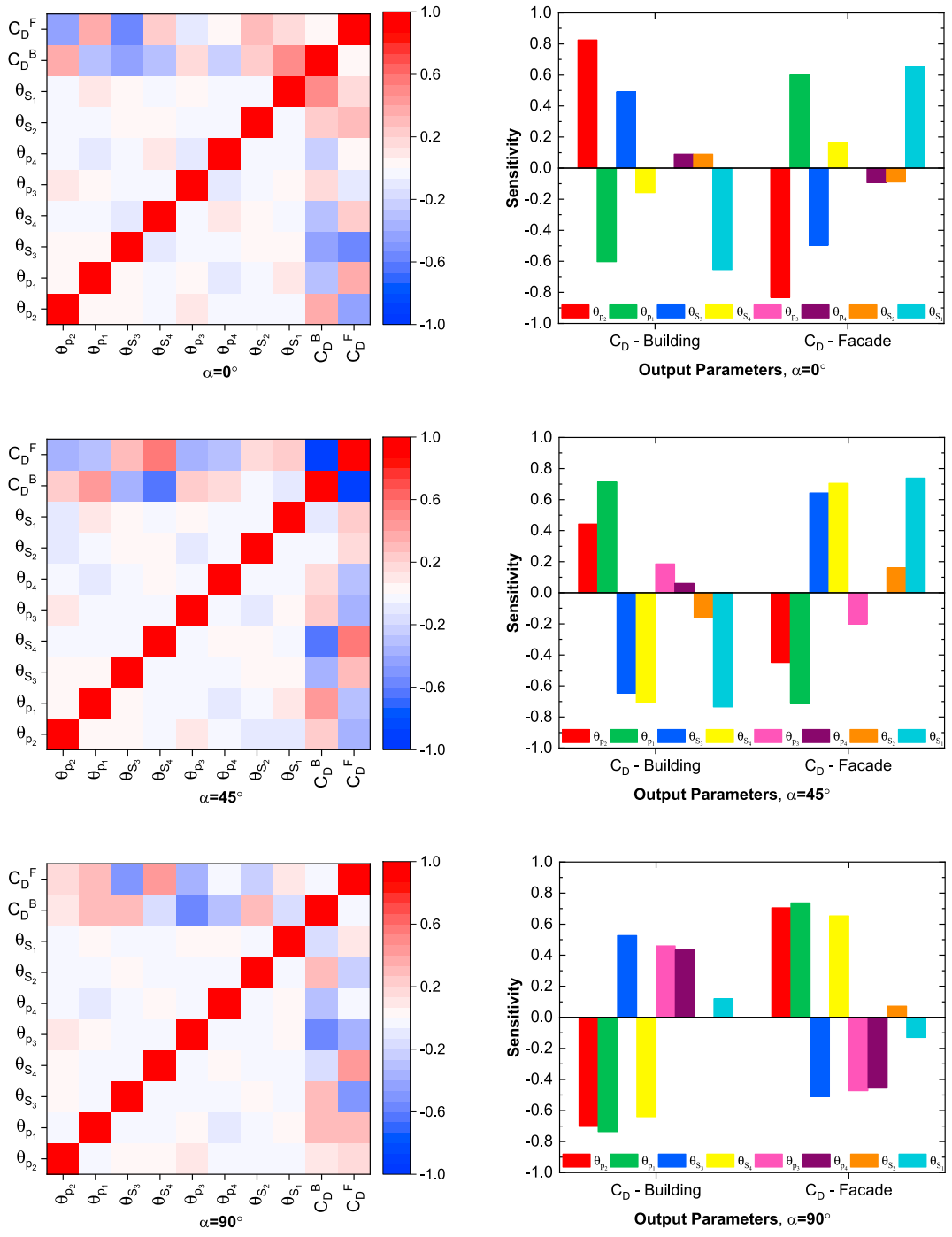

Fig. 15. Correlation map and sensitivity analysis for design variables and response or output parameters.

in Appendix-Figure A3. Careful examination of these plots reveals that the drag coefficients acting on building and façade are negatively correlated for most cases, and more correlation can be observed for lower angles of attack. With respect to sensitivity analysis, there is a random trend for the sensitivity of drag forces against twist angles, and it seems a nonlinear dependency between quantities exists, making the system more unpredictable. This makes use of the response surface model and the Genetic algorithm an excellent choice for predicting aerodynamic behavior and optimize such a complex system.

From an aerodynamic perspective, since double façades are intended to either reduce wind-induced loads or concentrate distributed wind loads on specific locations to control such forces, the goal here is to minimize the drag on only building and both façade and building. Fig. 16a illustrates the results obtained by reducing only C_D^B, and Fig. 16a shows the optimization results for simultaneously minimizing C_D^B and C_D^F. Comparison of Figs. 14 and 16 shows that, although the drag force has been reduced by twisting the façades at specific points, their overall impact on aerodynamic modification is not as significant as that of the parameters investigated in Step I. Fig. 16b demonstrates the possibility of significantly reducing the building's drag by minimizing only the building load (C_D^B), but the façade load increases instead, suggesting that the façade configuration shape strongly controls the drag. Depending on the objective function(s) and the project goals, it would be possible to reach a design for DSFs that provides the lowest force on the structure. Similar to the results in Fig. 14b, it is evident that a lower total drag force is achieved through minimization of both C_D^B and C_D^F compared to the optimization of onlyC_D^B.

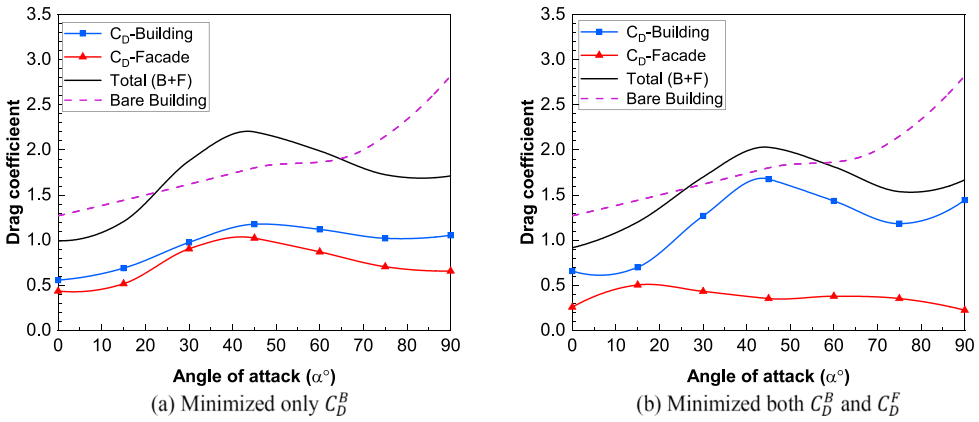

Fig. 16. Single and multi-objective optimization results after minimizing the drag coefficient for the rectangular façade (Step II).

6.2. EllipticAl double façade

This section focuses on the influence of the overall double-façade shape on the drag force. To this end, an elliptical shape was selected for streamlining the exterior shape and reducing the sudden flow separation around the corners of rectangular buildings. The façade geometry was parameterized by defining the B_W, B_L, D_L, D_W, as displayed in Fig. 3, enabling us to modify the geometry by changing these parameters. Central Composite Design (CCD) was again used here to determine the required sampling points, and this method accordingly proposed 25 sample points for each angle of attack to fit the RSM. As mentioned earlier, in performing the experiments at attack angles ranging from 0° to 90° in 10° increments, the total number of required numerical simulations was 250 (10 [angle] × 25 [sample]) cases. The sample points and drag coefficients obtained from CFD modeling for all attack angles are presented in Table 5.

Similar to the previous section for rectangular façades, the correlation map and sensitivity analysis are reported through separate graphs for each wind angle. Fig. 17 reveals a small dependency between design variables, and the plots for other angles are presented in Appendix-Figure A4. The drag coefficients are positively and negatively correlated with design variables and with one another. Although the correlation map exhibited a relatively random trend, among all other parameters, the variable B_L demonstrated a positive correlation with C_D^F and a negative correlation with C_D^B, with this correlation gradually vanishing with increasing angle of attack. The variable D_L also exhibited a positive relationship with C_D^F at the larger AOA that gradually disappears. From these two trends, it can be concluded that the major axis of the ellipse (B_L and D_L) has more influence on the DSF aerodynamics because increasing these axes lead to the generation of a streamlined body with a lower drag force. The relative sensitivity analysis indicates that all these design variables affect the aerodynamics of the double façade and building with different rates at a given α. Designing adaptive façades can take advantage of this sensitivity and provide the lowest aerodynamic force for a specific wind direction. The wind-induced response of tall buildings can also be controlled by installing an adaptive façade system with the capability for repositioning with variation in wind speed and direction.

Fig. 18 shows the results obtained from the single and multi-objective optimization problems solved by the NSGA-II algorithm. Depending on the approach used in the optimization algorithm, while it can be seen that the building drag force can be significantly reduced by modifying the façade shape, it should be noted that the building load reduction often causes an increase in the force magnitude acting on the façade, representing a tradeoff requirement. It should be noted that while this study has been conducted for only one wind speed or Reynolds number (Re), past studies indicate that the drag coefficient does not significantly change for an elliptical cylinder with Re less than 1.5×10^5 (Heddleson et al., 1957). The Reynolds number of tall buildings, varying with height due to changing wind speed, depends on the geometry and mean wind speed for specific terrain. Although the Reynolds number of tall buildings barely exceeds the critical value, its effect on the drag coefficient for different attack angles should be considered. Comparing the rectangular and elliptical façade results indicates that designing an elliptical façade is not noticeably effective in terms of reducing the wind-induced load for the design space tested here, and, depending on the attack angle, it may exhibit better or worse performance compared to the rectangular DSF, although it has a lower total drag coefficient for the multi-objective optimization cases. Given this result, it seems more reasonable to design rectangular-shaped DSFs because their manufacturing process is easier and cheaper than that of elliptical ones. It is interesting to observe that the façade drag becomes negative for specific design points because of the generated pressure gradient between the façade and building. As shown in Fig. 7b, there is a significant suction area with negative pressure inside the gap between the elliptical façade and building, while for the rectangular façade, the pressure inside the gap is mainly positive. This negative pressure could be due to a larger gap for the elliptical façade or its more streamlined shape than that of the rectangular façade. As a result, while this suction pressure results in a negative drag force, the integral of pressure distribution around the façade, the total force on the façade and building is positive. Depending on the façade geometry, the drag coefficient on the elliptical façade can be negative or positive. For example, the drag coefficient is positive for the case focused on minimizing the drag force only for the building (see Fig. 18a).

7. Conclusions

Over the past few decades, double skin façades have been mostly designed to improve indoor climate, save energy, and block sunlight. While there is convincing evidence that DSFs could also be used for reducing wind-induced loads on structures, there is still a lack of coherent research studying the effect of façade shape on wind-induced load and response of tall buildings at different angles of attack. Considering the large number of buildings worldwide that utilize DSFs, there would seem to be a business-related justification to enhance such functionality by integrating wind load-reducing features.

This paper utilized a holistic methodology that integrates statistical tools such as DOE and RSM and RANS-based CFD models of the building validated with experimental results to investigate the applicability of DSFs in reducing wind loads on tall buildings. It also presents numerical and optimization analyses for double façades with rectangular and elliptical shapes. For the rectangular façade, the optimal shape was found through steps I and II described in Section 6.1. The same process was carried out for an elliptical DSF using only one step because the influence of the elliptical façade was deemed so small that a second analysis was not conducted for it. Correlation maps and sensitivity analyses were presented for each angle of attack to demonstrate each design variable's

Table 5
Drag coefficients of the elliptical façade using CFD simulation.

	Façade Parameter (mm)				Attack Angle α°, $\frac{C_D Building}{C_D Facade}$									
Run	B_W	B_L	D_L	D_W	0°	10°	20°	30°	40°	50°	60°	70°	80°	90°
1	197.5	500.0	450.0	270.0	0.85	0.88	0.94	1.22	1.43	1.43	1.39	1.56	1.61	1.76
					0.09	0.22	0.40	0.66	0.55	0.60	0.48	0.20	0.15	0.23
2	185.0	500.0	450.0	270.0	1.06	1.06	1.35	1.49	1.82	2.00	1.62	1.77	2.06	1.89
					−0.13	−0.11	0.09	0.22	0.28	0.28	0.24	0.08	0.06	0.19
3	210.0	500.0	450.0	270.0	0.71	0.72	0.72	0.98	1.19	1.27	1.36	1.72	1.54	1.73
					0.27	0.43	0.62	0.71	0.76	0.73	0.54	0.14	0.10	0.17
4	197.5	450.0	450.0	270.0	0.90	0.96	0.98	1.26	1.55	1.58	1.94	1.75	1.95	1.99
					−0.12	0.04	0.25	0.39	0.43	0.47	0.29	0.11	0.04	0.07
5	197.5	550.0	450.0	270.0	0.76	0.78	0.97	1.10	1.35	1.54	1.37	1.67	1.74	1.88
					0.25	0.36	0.48	0.63	0.63	0.64	0.52	0.23	0.10	0.21
6	197.5	500.0	350.0	270.0	0.97	1.00	1.17	1.36	1.63	1.77	1.62	1.68	1.89	1.97
					−0.03	0.05	0.24	0.39	0.30	0.29	0.13	−0.10	−0.25	−0.49
7	197.5	500.0	550.0	270.0	0.82	0.85	0.92	1.15	1.36	1.60	1.54	1.53	1.45	1.65
					0.09	0.25	0.42	0.61	0.64	0.67	0.58	0.29	0.38	0.43
8	197.5	500.0	450.0	260.0	0.90	0.93	1.07	1.38	1.57	1.72	1.73	1.58	1.81	1.85
					0.13	0.17	0.34	0.45	0.36	0.34	0.21	0.03	−0.12	−0.03
9	197.5	500.0	450.0	280.0	0.81	0.84	0.98	1.09	1.28	1.46	1.35	1.25	1.58	1.67
					0.03	0.19	0.39	0.65	0.70	0.74	0.66	0.40	0.33	0.43
10	188.7	464.8	379.6	263.0	1.08	1.17	1.28	1.54	1.79	1.98	1.73	1.90	2.15	2.25
					−0.14	−0.13	0.02	0.15	0.08	0.09	0.03	−0.16	−0.31	−0.24
11	206.3	464.8	379.6	263.0	1.00	1.10	1.19	1.46	1.64	1.97	2.15	1.76	2.27	2.05
					−0.03	0.11	0.29	0.37	0.23	0.16	−0.07	−0.17	−0.44	−0.40
12	188.7	535.2	379.6	263.0	1.02	1.04	1.23	1.51	1.86	1.98	1.73	1.82	1.96	2.26
					0.02	0.01	0.11	0.23	0.12	0.10	0.07	−0.16	−0.23	−0.25
13	206.3	535.2	379.6	263.0	1.04	1.10	1.29	1.48	1.74	1.78	1.80	1.91	2.16	2.12
					0.11	0.16	0.29	0.40	0.29	0.29	0.04	−0.20	−0.43	−0.47
14	188.7	464.8	520.4	263.0	1.07	1.08	1.31	1.52	1.78	1.83	2.13	1.90	2.02	2.14
					−0.16	−0.11	0.06	0.20	0.18	0.17	0.14	−0.05	0.13	0.10
15	206.3	464.8	520.4	263.0	0.75	0.80	0.83	1.09	1.39	1.63	1.53	1.47	1.54	1.85
					0.14	0.34	0.50	0.73	0.56	0.55	0.44	0.20	0.13	0.12
16	188.7	535.2	520.4	263.0	0.90	0.91	1.10	1.38	1.60	1.65	1.63	1.64	1.51	1.76
					0.11	0.11	0.29	0.43	0.42	0.45	0.35	0.15	0.31	0.23
17	206.3	535.2	520.4	263.0	0.69	0.71	0.81	1.11	1.30	1.42	1.42	1.67	1.79	1.93
					0.39	0.45	0.60	0.81	0.75	0.67	0.52	0.13	0.08	0.16
18	188.7	464.8	379.6	277.0	1.04	1.15	1.15	1.45	1.73	1.87	1.87	2.15	2.02	1.89
					−0.23	−0.15	0.07	0.27	0.21	0.29	0.28	−0.04	−0.08	0.07
19	206.3	464.8	379.6	277.0	0.74	0.83	0.88	1.00	1.22	1.26	1.45	1.41	1.62	1.65
					0.07	0.25	0.48	0.67	0.66	0.62	0.47	0.23	0.04	−0.18
20	188.7	535.2	379.6	277.0	0.90	0.95	1.15	1.29	1.45	1.42	1.61	1.70	1.83	1.73
					0.02	0.07	0.28	0.43	0.46	0.54	0.47	0.18	0.08	0.13
21	206.3	535.2	379.6	277.0	0.72	0.73	0.89	1.01	1.25	1.43	1.23	1.31	1.51	1.67
					0.25	0.38	0.55	0.70	0.74	0.71	0.56	0.24	0.05	−0.18
22	188.7	464.8	520.4	277.0	1.06	1.14	1.38	1.47	1.75	1.90	1.84	1.89	2.10	2.07
					−0.25	−0.14	0.06	0.31	0.28	0.27	0.26	0.16	0.17	0.25
23	206.3	464.8	520.4	277.0	0.74	0.82	0.72	0.97	1.20	1.26	1.25	1.26	1.46	1.77
					0.07	0.27	0.55	0.77	0.77	0.83	0.71	0.46	0.38	0.44
24	188.7	535.2	520.4	277.0	0.94	0.88	1.14	1.33	1.59	1.49	1.51	1.43	1.92	1.73
					0.01	0.08	0.33	0.50	0.64	0.61	0.60	0.37	0.41	0.54
25	206.3	535.2	520.4	277.0	0.69	0.70	0.72	0.89	1.15	1.21	1.30	1.48	1.52	1.27
					0.30	0.40	0.68	0.86	1.00	0.97	0.90	0.47	0.48	0.71

impact on the drag coefficient of the building and façade, with results that show that the opening or façade length and gap between the façade and building can significantly affect a tall building's aerodynamics. Since it was also found that the elliptical façade tested here provides aerodynamic performance quite similar to that of the rectangular façade, the greater simplicity of rectangular façade construction makes this shape a better choice for practical applications while still providing satisfactory aerodynamic performance.

The results from the research substantiate the hypothesis that DSFs can significantly transfer the load from the building to the façade system by distributing airflow into low-pressure areas. Apart from other features, based on the results presented, a double façade can be classified as an aerodynamic modification approach for both existing high-rise buildings and new designs. The unique approach considered in this study, accounting for different attack angles, highlights the fact that different AOAs would result in different optimized façade shapes. This leads to the perfect business justification for the use of smart morphing façades (Smorphacades) that can change their configuration depending on the angle of the wind to minimize wind-induced loads. The results presented here prove that integrating such an adaptive system with an optimization-based control system could result in an excellent system for reducing or transferring the load from building to façade or vice versa.

The extracted parameter of interest from CFD models was the drag coefficient. The reduction of drag coefficients, as conducted through the optimization model in this manuscript, will result in lowering the external loads in the along wind direction of the tall building. This by itself is an important factor from the perspective of efficiency in the structural design of tall buildings. However, crosswind-induced vibrations that could impact other performance objectives such as occupant comfort play an important role in the final design and proportioning of the structural components of a tall building. While the proposed methodology was successful in streamlining a process to optimize the drag

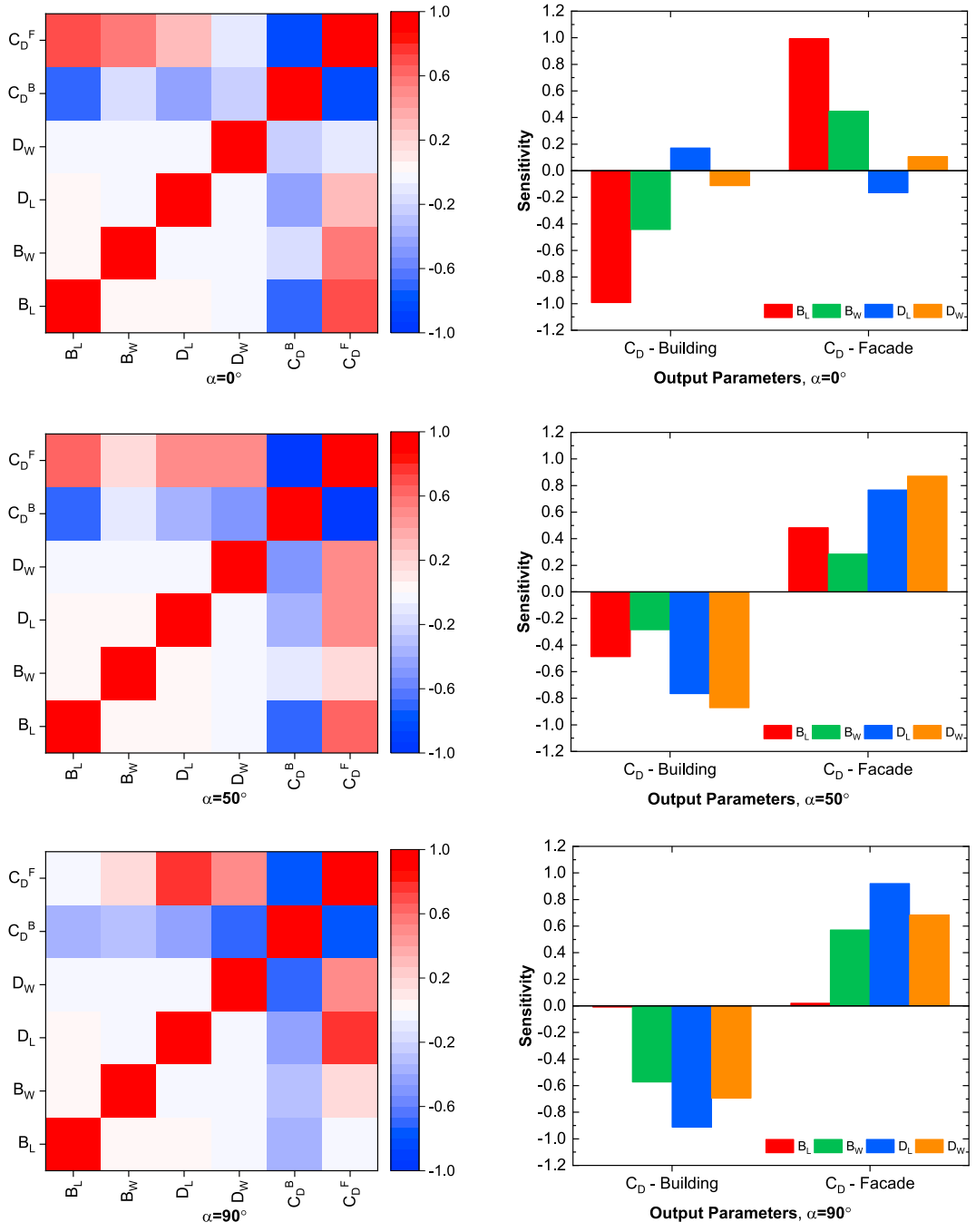

Fig. 17. Correlation map and sensitivity analysis for the elliptical double façade.

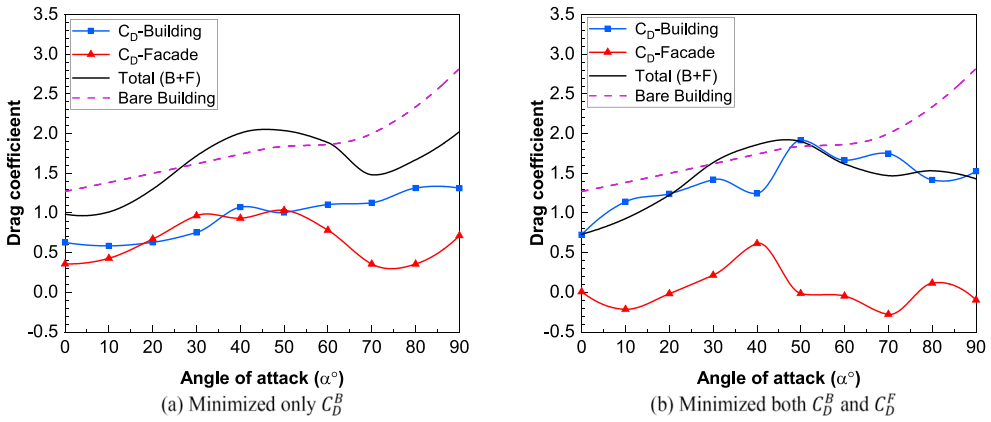

Fig. 18. Single and multi-objective optimization results after minimizing the drag for building with the elliptical façade.

coefficients, it is expected that future studies currently underway by the authors will enhance its applicability in two major ways: 1) consideration of high-fidelity CFD models that account for not only across wind drag coefficients and along-wind vibrations but also the consideration of local wind pressure changes across the moving façade, and 2) conducting aeroelastic wind tunnel experiments on the buildings with the Smorphacades.

As mentioned in the earlier sections of the paper, because of the large computational effort required to create a sufficient design space, while only a 2D CFD simulation was considered here, it would be plausible in future extensions of this work to consider three-dimensional flow effects and to measure load under the atmospheric boundary layer wind profile to confirm the aerodynamic efficiency of double-skin façades. Furthermore, more research would be required to evaluate the aerodynamic performance of façades for other building shapes. Due to the limitation of wind tunnel experiments on testing such complex models, the CFD technique could overcome these limitations and provide a better intuitive grasp of the fluid dynamics of double façades. In this regard, high-fidelity turbulence models such as large eddy simulation (LES) or detached eddy simulation (DES) could be used to accurately capture the flow around the façade.

CRediT authorship contribution statement

Mohammad Jafari: Methodology, Validation, Formal analysis, Investigation, Data curation, Writing – original draft, Visualization. **Alice Alipour:** Conceptualization, Methodology, Investigation, Writing – review & editing, Supervision, Project administration, Funding acquisition.

Declaration of competing interest

The authors declare that they have no known competing financial interests or personal relationships that could have appeared to influence the work reported in this paper.

Acknowledgment

This paper is based upon work supported by the National Science Foundation under Grant No. 1826356. Their support is gratefully acknowledged. Any opinions, findings, and conclusions or recommendations expressed in this material are those of the authors and do not necessarily reflect the sponsor' 's views.

Appendix

The sampling points used for optimization Step II of the rectangular façade are shown in Table A1. The CFD results obtained for these sampling points are presented in Table A2.

Table A1
Sample points using the Latin Hypercube Sampling method for twisting rectangular façades (all units are degree).

SP	θ_{S_1}	θ_{S_2}	θ_{S_3}	θ_{S_4}	θ_{P_1}	θ_{P_2}	θ_{P_3}	θ_{P_4}	SP	θ_{S_1}	θ_{S_2}	θ_{S_3}	θ_{S_4}	θ_{P_1}	θ_{P_2}	θ_{P_3}	θ_{P_4}
1	−27.4	−20.7	−11.9	6.7	18.5	−11.1	−25.2	−9.6	**42**	23.0	−29.6	−20.0	−25.2	17.8	−9.6	−11.1	−2.2
2	5.9	20.0	11.9	25.2	−2.2	1.5	6.7	23.0	**43**	−8.9	16.3	5.2	−15.6	−11.1	5.9	−21.5	−6.7
3	−12.6	−22.2	19.3	28.1	15.6	−28.9	−20.7	15.6	**44**	18.5	24.4	17.8	−18.5	−20.0	−22.2	15.6	−17.0
4	−14.8	−28.1	−6.7	−20.0	19.3	−5.9	7.4	−28.1	**45**	−21.5	−8.9	11.1	3.7	0.7	11.9	−15.6	−25.9
5	−1.5	13.3	−25.9	−2.2	−25.9	−26.7	29.6	0.7	**46**	−23.0	3.0	−20.7	−10.4	9.6	6.7	18.5	−26.7
6	−6.7	17.0	20.0	−4.4	6.7	25.2	−24.4	−15.6	**47**	−16.3	12.6	−8.1	−17.0	−15.6	18.5	2.2	−23.0
7	25.9	7.4	−17.0	5.9	−7.4	−8.9	5.9	25.9	**48**	−29.6	−25.2	10.4	21.5	−28.1	3.7	−18.5	−7.4
8	−20.7	2.2	15.6	−29.6	−27.4	24.4	−20.0	8.9	**49**	−7.4	20.7	−16.3	17.8	3.7	−20.0	16.3	20.7
9	11.1	−8.1	20.7	8.9	24.4	−21.5	−5.9	8.1	**50**	20.0	8.9	13.3	−24.4	−9.6	−29.6	−17.0	1.5
10	21.5	−0.7	26.7	−16.3	−10.4	−24.4	−5.2	28.9	**51**	−5.2	−25.9	8.9	14.8	−23.7	−23.7	−19.3	−16.3
11	0.0	−11.1	16.3	−14.1	23.7	−16.3	20.0	5.2	**52**	−25.2	−11.9	2.2	24.4	5.2	11.1	8.1	16.3
12	23.7	10.4	−14.1	−8.1	−18.5	−25.2	−13.3	0.0	**53**	−13.3	−10.4	−24.4	−5.9	20.7	19.3	−14.8	29.6
13	24.4	−5.9	29.6	−12.6	−13.3	−13.3	5.2	−14.1	**54**	14.1	−4.4	−18.5	−26.7	7.4	8.1	25.9	−21.5
14	−28.1	8.1	−4.4	2.2	−14.1	5.2	10.4	7.4	**55**	9.6	−20.0	1.5	−27.4	−21.5	−11.9	−9.6	−0.7
15	−17.0	0.0	−7.4	28.9	14.8	−18.5	28.1	3.0	**56**	−14.1	29.6	24.4	−0.7	1.5	−7.4	0.7	5.9
16	16.3	−18.5	12.6	−8.9	−19.3	15.6	−2.2	19.3	**57**	8.1	5.2	−23.0	−5.2	10.4	14.8	24.4	−11.9
17	15.6	19.3	23.7	11.9	2.2	13.3	−12.6	−25.2	**58**	12.6	17.8	−21.5	26.7	−5.9	9.6	−25.9	−24.4
18	26.7	−3.0	−13.3	23.0	11.9	0.0	−4.4	11.1	**59**	−11.1	−28.9	−10.4	−14.8	17.0	−8.1	3.7	6.7

(*continued on next column*)

Table A1 (*continued*)

SP	θ_{S_1}	θ_{S_2}	θ_{S_3}	θ_{S_4}	θ_{P_1}	θ_{P_2}	θ_{P_3}	θ_{P_4}	SP	θ_{S_1}	θ_{S_2}	θ_{S_3}	θ_{S_4}	θ_{P_1}	θ_{P_2}	θ_{P_3}	θ_{P_4}
19	−4.4	−26.7	22.2	−13.3	3.0	−25.9	13.3	−5.2	**60**	17.8	−27.4	−0.7	4.4	−8.9	28.1	1.5	−11.1
20	−19.3	18.5	−28.1	−3.0	22.2	−27.4	11.9	−3.7	**61**	−8.1	0.7	−29.6	25.9	−5.2	−28.1	8.9	−27.4
21	17.0	27.4	−9.6	0.7	−3.7	−14.1	−10.4	−12.6	**62**	−3.0	−23.0	−27.4	−6.7	−17.8	0.7	−26.7	9.6
22	−24.4	−12.6	−25.2	14.1	−24.4	16.3	−7.4	13.3	**63**	−22.2	28.9	3.0	−3.7	20.0	−1.5	−29.6	22.2
23	−20.0	25.9	25.9	1.5	28.9	27.4	−1.5	12.6	**64**	6.7	1.5	9.6	5.2	27.4	23.7	−27.4	−23.7
24	−0.7	−2.2	−3.0	16.3	−22.2	−23.0	0.0	14.8	**65**	5.2	−6.7	6.7	22.2	26.7	−12.6	−3.0	11.9
25	7.4	14.1	−12.6	−1.5	4.4	7.4	−28.9	−10.4	**66**	20.7	23.0	28.9	8.1	−8.1	20.7	−16.3	23.7
26	−18.5	6.7	21.5	−23.0	28.1	−0.7	14.1	−20.7	**67**	3.7	−15.6	−3.7	27.4	−29.6	2.2	21.5	17.8
27	−9.6	−7.4	23.0	20.0	−28.9	12.6	11.1	−4.4	**68**	1.5	26.7	−2.2	17.0	25.2	25.9	25.2	18.5
28	−26.7	3.7	8.1	12.6	−14.8	4.4	−3.7	−1.5	**69**	−11.9	11.1	25.2	−11.1	8.1	−4.4	23.7	17.0
29	4.4	−16.3	−5.2	11.1	−16.3	28.9	−11.9	−8.9	**70**	19.3	−1.5	−8.9	−22.2	−25.2	26.7	19.3	27.4
30	22.2	11.9	−14.8	−7.4	−26.7	−15.6	−22.2	−19.3	**71**	−3.7	−14.1	3.7	13.3	−11.9	8.9	−0.7	21.5
31	27.4	−9.6	0.0	23.7	−4.4	10.4	4.4	2.2	**72**	13.3	28.1	14.1	−23.7	5.9	−17.0	9.6	4.4
32	14.8	21.5	−11.1	−11.9	−12.6	14.1	−6.7	10.4	**73**	29.6	−23.7	5.9	19.3	25.9	23.0	27.4	−5.9
33	0.7	4.4	7.4	29.6	−3.0	−10.4	3.0	−20.0	**74**	3.0	−19.3	4.4	−17.8	14.1	−19.3	−23.0	−13.3
34	10.4	−24.4	28.1	18.5	29.6	17.0	−8.9	−3.0	**75**	−25.9	15.6	17.0	−9.6	−23.0	3.0	−8.1	25.2
35	−15.6	−3.7	−1.5	−21.5	21.5	−14.8	23.0	24.4	**76**	28.9	9.6	18.5	20.7	−0.7	−3.0	20.7	−29.6
36	−23.7	−17.0	27.4	−19.3	−17.0	−20.7	22.2	−17.8	**77**	8.9	14.8	−22.2	0.0	8.9	−6.7	12.6	28.1
37	−2.2	−14.8	−15.6	−28.1	23.0	21.5	17.8	3.7	**78**	−28.9	23.7	−28.9	10.4	13.3	−17.8	−14.1	−14.8
38	−5.9	22.2	0.7	−28.9	0.0	20.0	14.8	−8.1	**79**	11.9	25.2	−19.3	9.6	11.1	−5.2	−28.1	−18.5
39	2.2	−17.8	−17.8	−25.9	12.6	−2.2	−23.7	20.0	**80**	−10.4	−13.3	14.8	15.6	−6.7	17.8	28.9	−28.9
40	25.2	5.9	−26.7	−20.7	−1.5	29.6	17.0	−22.2	**81**	−17.8	−5.2	−23.7	7.4	−20.7	22.2	26.7	14.1
41	28.1	−21.5	−5.9	3.0	16.3	−3.7	−17.8	26.7									

Table A2
Numerical results of drag coefficients obtained for the elliptical façade.

Run	$\alpha = 0°$		$\alpha = 15°$		$\alpha = 30°$		$\alpha = 45°$		$\alpha = 60°$		$\alpha = 75°$		$\alpha = 90°$	
	C_D^B	C_D^F	C_D^B	C_D^F	C_D^B	C_D^F	C_D^B	C_D^F	C_D^B	C_D^F	C_D^B	C_D^F	C_D^B	C_D^F
1	0.61	0.43	0.90	0.37	1.25	0.52	1.65	0.57	1.69	0.62	1.53	0.58	1.30	0.65
2	0.66	0.43	0.71	0.50	1.04	0.83	1.31	0.89	1.40	0.85	1.38	0.62	1.40	0.66
3	0.62	0.37	0.85	0.44	1.19	0.70	1.45	0.81	1.65	0.78	1.39	0.64	1.46	0.63
4	0.63	0.41	0.98	0.30	1.46	0.36	1.80	0.35	1.74	0.40	1.33	0.41	1.34	0.61
5	0.69	0.40	0.89	0.36	1.32	0.54	1.82	0.46	1.78	0.45	1.35	0.44	1.56	0.62
6	0.66	0.35	0.86	0.37	1.32	0.63	1.72	0.67	1.87	0.57	1.58	0.46	1.20	0.71
7	0.71	0.40	0.90	0.44	1.35	0.54	1.73	0.48	1.57	0.70	1.37	0.59	1.24	0.64
8	0.69	0.27	0.90	0.39	1.31	0.51	1.53	0.62	1.78	0.64	1.27	0.54	1.34	0.61
9	0.63	0.43	0.88	0.47	1.15	0.69	1.53	0.76	1.42	0.69	1.32	0.59	1.36	0.68
10	0.66	0.37	0.84	0.49	1.15	0.73	1.46	0.78	1.50	0.69	1.44	0.56	1.54	0.61
11	0.59	0.40	0.90	0.38	1.36	0.55	1.77	0.58	1.62	0.48	1.20	0.50	1.27	0.61
12	0.69	0.44	0.90	0.43	1.36	0.68	1.79	0.67	1.40	0.58	1.61	0.52	1.54	0.62
13	0.70	0.37	0.84	0.39	1.12	0.75	1.36	0.86	1.59	0.75	1.26	0.61	1.21	0.66
14	0.66	0.39	0.95	0.41	1.36	0.53	1.61	0.58	1.46	0.64	1.49	0.63	1.22	0.66
15	0.60	0.41	0.80	0.44	1.29	0.52	1.52	0.62	1.77	0.65	1.09	0.55	1.18	0.65
16	0.70	0.29	1.06	0.34	1.25	0.57	1.60	0.63	1.54	0.60	1.30	0.62	1.49	0.68
17	0.71	0.39	0.96	0.38	1.17	0.76	1.50	0.88	1.41	0.76	1.55	0.59	1.48	0.69
18	0.72	0.41	0.80	0.42	1.25	0.53	1.47	0.70	1.27	0.69	1.43	0.63	1.55	0.57
19	0.61	0.40	0.80	0.42	1.27	0.63	1.62	0.70	1.39	0.64	1.50	0.57	1.47	0.65
20	0.69	0.40	1.00	0.35	1.49	0.43	1.82	0.39	1.87	0.41	1.23	0.43	1.52	0.61
21	0.69	0.48	0.98	0.44	1.27	0.81	1.56	0.83	1.80	0.76	1.47	0.61	1.64	0.60
22	0.76	0.32	1.00	0.34	1.45	0.45	1.59	0.59	1.49	0.64	1.42	0.67	1.70	0.39
23	0.68	0.31	0.87	0.36	1.51	0.42	1.84	0.49	1.94	0.42	1.27	0.43	1.59	0.50
24	0.60	0.40	0.74	0.50	1.22	0.75	1.43	0.78	1.32	0.71	1.41	0.68	1.26	0.65
25	0.62	0.46	0.87	0.38	1.32	0.64	1.66	0.64	1.64	0.57	1.62	0.48	1.50	0.58
26	0.63	0.34	0.87	0.32	1.43	0.42	1.75	0.38	1.65	0.36	1.60	0.41	1.60	0.55
27	0.67	0.32	0.89	0.38	1.18	0.64	1.47	0.77	1.62	0.79	1.13	0.71	1.44	0.61
28	0.64	0.37	0.77	0.50	1.14	0.64	1.47	0.81	1.58	0.77	1.02	0.72	1.42	0.69
29	0.64	0.36	0.97	0.33	1.25	0.64	1.46	0.75	1.48	0.76	1.24	0.73	1.49	0.69
30	0.68	0.43	0.88	0.40	1.30	0.73	1.73	0.67	1.97	0.63	1.37	0.47	1.53	0.61
31	0.70	0.41	0.89	0.38	1.19	0.67	1.31	0.82	1.47	0.79	1.20	0.67	1.41	0.62
32	0.71	0.46	0.84	0.37	1.29	0.58	1.69	0.55	1.53	0.50	1.20	0.51	1.47	0.60
33	0.59	0.45	0.77	0.45	1.14	0.77	1.32	1.00	1.52	0.97	1.33	0.71	1.63	0.60
34	0.69	0.38	1.02	0.27	1.32	0.52	1.46	0.72	1.29	0.72	1.08	0.62	1.32	0.58
35	0.63	0.42	0.87	0.37	1.49	0.35	1.88	0.38	1.98	0.41	1.28	0.46	1.46	0.56
36	0.66	0.35	0.80	0.40	1.23	0.64	1.54	0.70	1.40	0.63	1.14	0.58	1.56	0.53
37	0.70	0.40	1.13	0.20	1.73	0.20	1.96	0.27	2.01	0.36	1.21	0.48	1.48	0.58
38	0.66	0.43	0.93	0.32	1.35	0.46	1.74	0.45	1.93	0.43	1.39	0.47	1.41	0.53
39	0.63	0.45	1.02	0.34	1.42	0.42	1.72	0.49	1.62	0.46	1.23	0.47	1.52	0.58
40	0.75	0.37	1.05	0.18	1.47	0.36	1.83	0.34	1.73	0.43	1.23	0.47	1.56	0.49
41	0.68	0.44	0.88	0.34	1.28	0.63	1.65	0.67	1.42	0.63	1.28	0.56	1.51	0.57
42	0.73	0.44	0.91	0.30	1.38	0.52	1.85	0.53	1.69	0.53	1.39	0.52	1.36	0.63
43	0.62	0.40	0.83	0.46	1.27	0.64	1.59	0.70	1.62	0.62	1.63	0.46	1.33	0.68
44	0.72	0.35	0.89	0.43	1.14	0.76	1.58	0.68	1.79	0.62	1.23	0.51	1.18	0.71

(*continued on next column*)

Table A2 (*continued*)

Run	$\alpha = 0°$		$\alpha = 15°$		$\alpha = 30°$		$\alpha = 45°$		$\alpha = 60°$		$\alpha = 75°$		$\alpha = 90°$	
	C_D^B	C_D^F	C_D^B	C_D^F	C_D^B	C_D^F	C_D^B	C_D^F	C_D^B	C_D^F	C_D^B	C_D^F	C_D^B	C_D^F
45	0.62	0.35	0.94	0.41	1.33	0.59	1.54	0.70	1.64	0.62	1.61	0.63	1.55	0.56
46	0.67	0.37	1.09	0.25	1.55	0.19	2.02	0.13	2.03	0.22	1.57	0.39	1.36	0.57
47	0.71	0.37	0.94	0.32	1.42	0.42	1.66	0.50	1.49	0.48	1.65	0.53	1.49	0.61
48	0.65	0.34	0.94	0.41	1.11	0.71	1.34	0.85	1.50	0.86	1.39	0.71	1.27	0.61
49	0.64	0.43	0.77	0.44	1.22	0.61	1.70	0.67	1.82	0.66	1.46	0.62	1.59	0.52
50	0.70	0.35	0.79	0.49	1.19	0.82	1.61	0.79	1.69	0.68	1.58	0.51	1.56	0.50
51	0.63	0.36	0.76	0.48	1.02	0.88	1.32	0.90	1.58	0.86	1.55	0.72	1.44	0.56
52	0.61	0.39	0.81	0.39	1.39	0.50	1.65	0.56	1.75	0.55	1.39	0.61	1.48	0.66
53	0.69	0.37	0.91	0.33	1.67	0.29	1.91	0.31	1.72	0.38	1.43	0.52	1.31	0.68
54	0.68	0.44	0.98	0.26	1.42	0.37	1.87	0.41	2.01	0.42	1.49	0.43	1.61	0.55
55	0.67	0.39	0.85	0.36	1.26	0.75	1.60	0.73	1.45	0.67	1.45	0.59	1.53	0.59
56	0.65	0.37	0.89	0.49	1.22	0.62	1.51	0.73	1.72	0.64	1.22	0.49	1.54	0.55
57	0.67	0.43	1.07	0.25	1.40	0.42	1.92	0.30	1.88	0.38	1.42	0.48	1.62	0.61
58	0.74	0.41	0.94	0.37	1.32	0.71	1.33	0.89	1.28	0.85	1.36	0.62	1.37	0.63
59	0.65	0.42	0.88	0.31	1.56	0.34	1.82	0.33	1.87	0.40	1.44	0.50	1.34	0.68
60	0.68	0.40	0.99	0.27	1.21	0.62	1.55	0.71	1.42	0.66	1.06	0.63	1.55	0.70
61	0.70	0.42	0.87	0.43	1.25	0.60	1.48	0.78	1.56	0.80	1.40	0.66	1.50	0.69
62	0.69	0.39	0.98	0.36	1.34	0.57	1.63	0.65	1.91	0.62	1.44	0.59	1.60	0.51
63	0.61	0.42	0.88	0.45	1.40	0.51	1.80	0.45	1.58	0.43	1.30	0.38	1.59	0.56
64	0.68	0.36	0.94	0.36	1.29	0.62	1.61	0.69	1.74	0.60	1.40	0.52	1.50	0.64
65	0.59	0.46	0.83	0.45	1.23	0.65	1.43	0.76	1.49	0.70	1.05	0.63	1.60	0.60
66	0.72	0.38	0.95	0.42	1.15	0.68	1.47	0.76	1.28	0.81	1.66	0.57	1.37	0.47
67	0.62	0.38	0.97	0.36	1.30	0.57	1.44	0.80	1.65	0.76	1.15	0.72	1.41	0.50
68	0.67	0.42	0.89	0.33	1.24	0.57	1.58	0.54	1.84	0.53	1.49	0.56	1.47	0.57
69	0.61	0.36	0.88	0.46	1.29	0.59	1.61	0.54	1.83	0.51	1.36	0.45	1.52	0.52
70	0.75	0.37	0.91	0.29	1.33	0.39	1.69	0.43	1.65	0.49	1.39	0.54	1.43	0.40
71	0.59	0.39	0.86	0.46	1.31	0.62	1.64	0.65	1.79	0.69	1.21	0.65	1.46	0.48
72	0.68	0.43	0.90	0.43	1.17	0.75	1.59	0.73	1.40	0.57	1.47	0.45	1.54	0.48
73	0.70	0.37	1.05	0.27	1.40	0.54	1.62	0.66	1.59	0.66	1.51	0.58	1.47	0.46
74	0.59	0.46	0.90	0.44	1.20	0.67	1.62	0.61	1.72	0.63	1.59	0.52	1.28	0.55
75	0.66	0.30	0.89	0.47	1.25	0.61	1.69	0.71	1.68	0.58	1.18	0.52	1.38	0.62
76	0.71	0.36	0.94	0.41	1.16	0.75	1.33	0.87	1.43	0.90	1.06	0.63	1.56	0.53
77	0.68	0.47	0.92	0.42	1.26	0.55	1.76	0.49	1.57	0.48	1.15	0.51	1.46	0.65
78	0.68	0.42	0.78	0.43	1.44	0.53	1.68	0.59	1.55	0.55	1.48	0.50	1.31	0.47
79	0.73	0.44	0.88	0.38	1.26	0.70	1.64	0.75	1.55	0.63	1.40	0.53	1.36	0.57
80	0.65	0.32	0.92	0.36	1.43	0.49	1.49	0.59	1.58	0.66	1.46	0.54	1.61	0.50
81	0.73	0.30	0.93	0.31	1.50	0.35	1.73	0.46	1.65	0.55	1.14	0.53	1.52	0.61

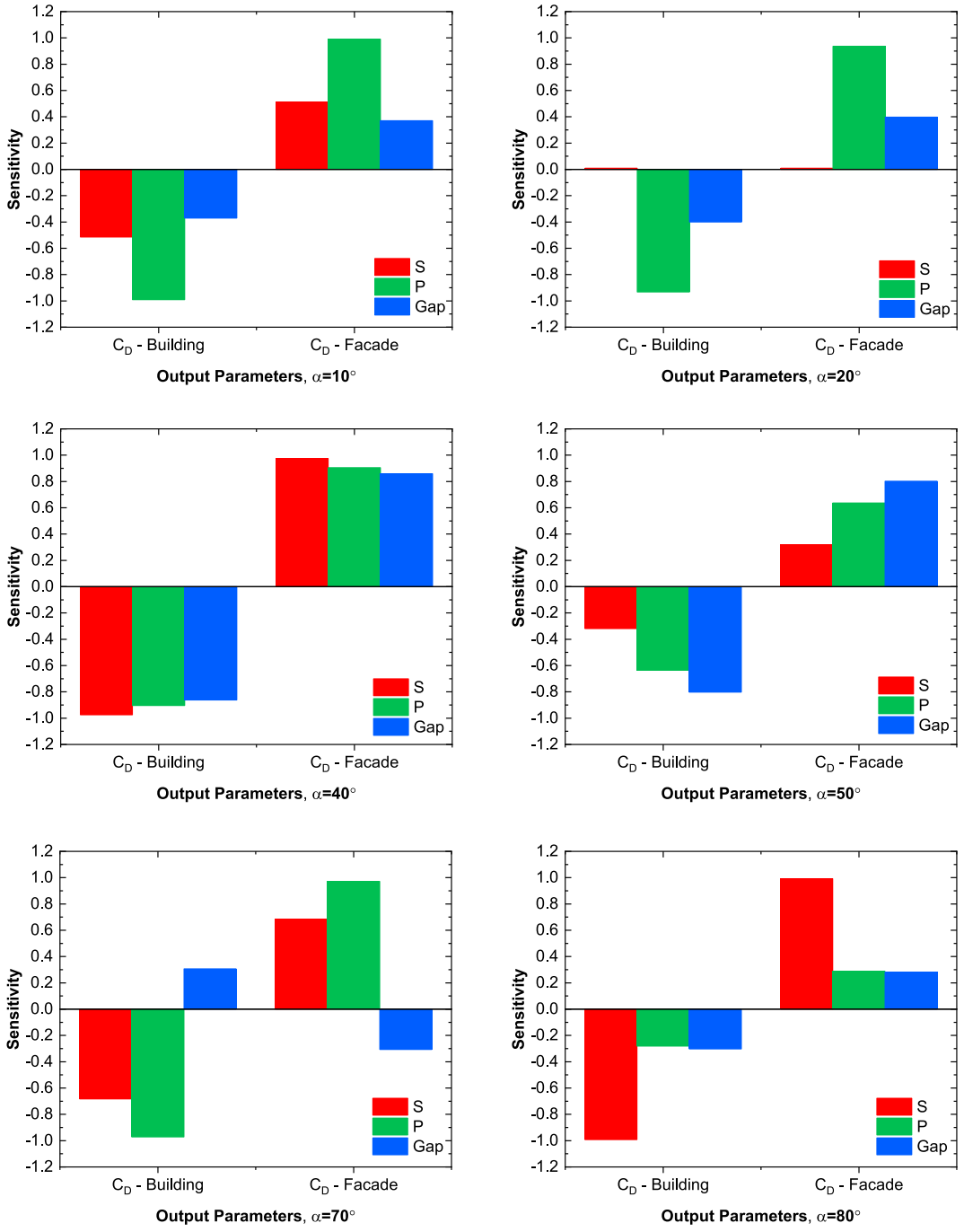

Fig. A1. Relative sensitivity of the drag coefficient of building and rectangular façade against design variables *S*, *P*, and Gap.

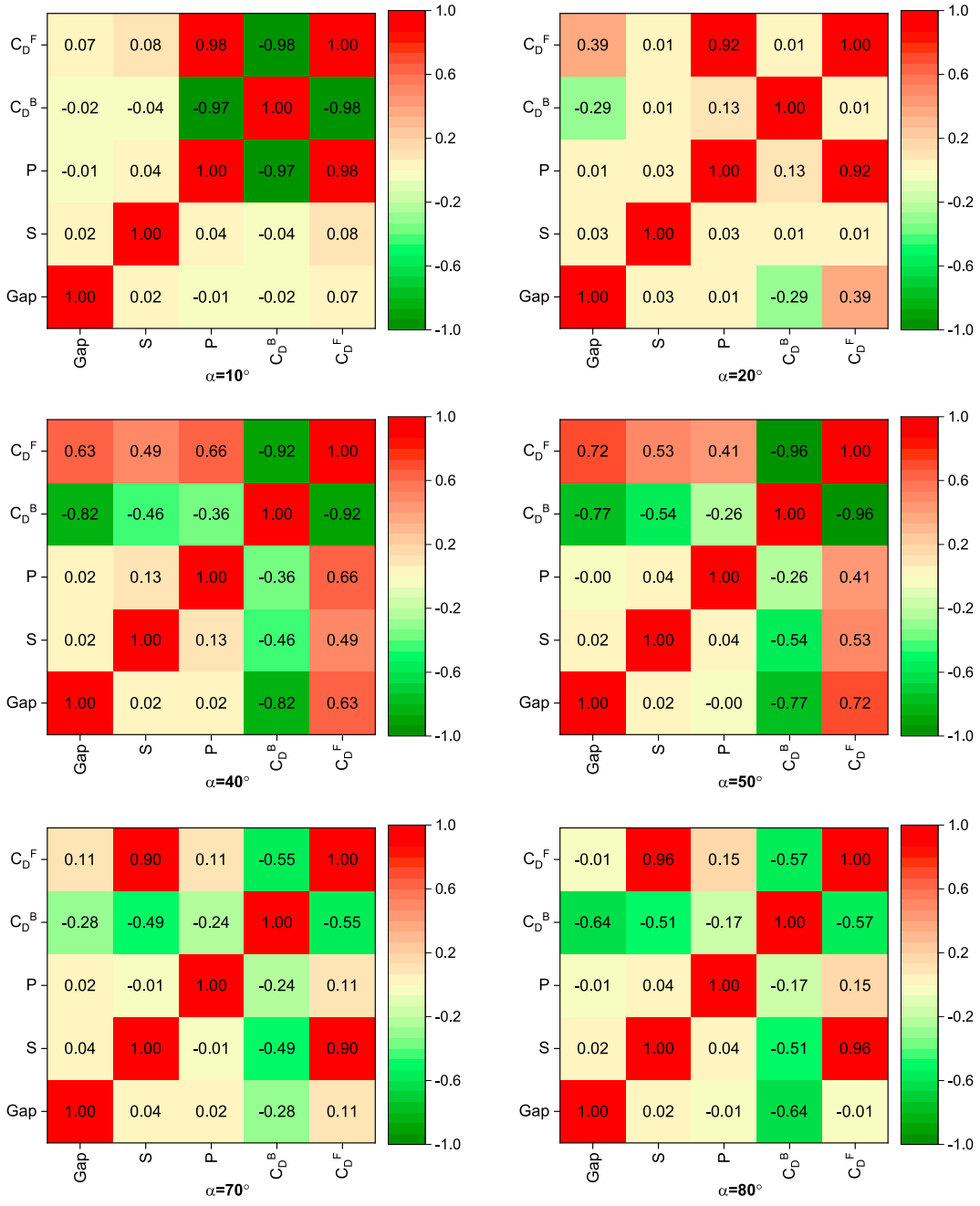

Fig. A2. Correlation map for design and response variables.

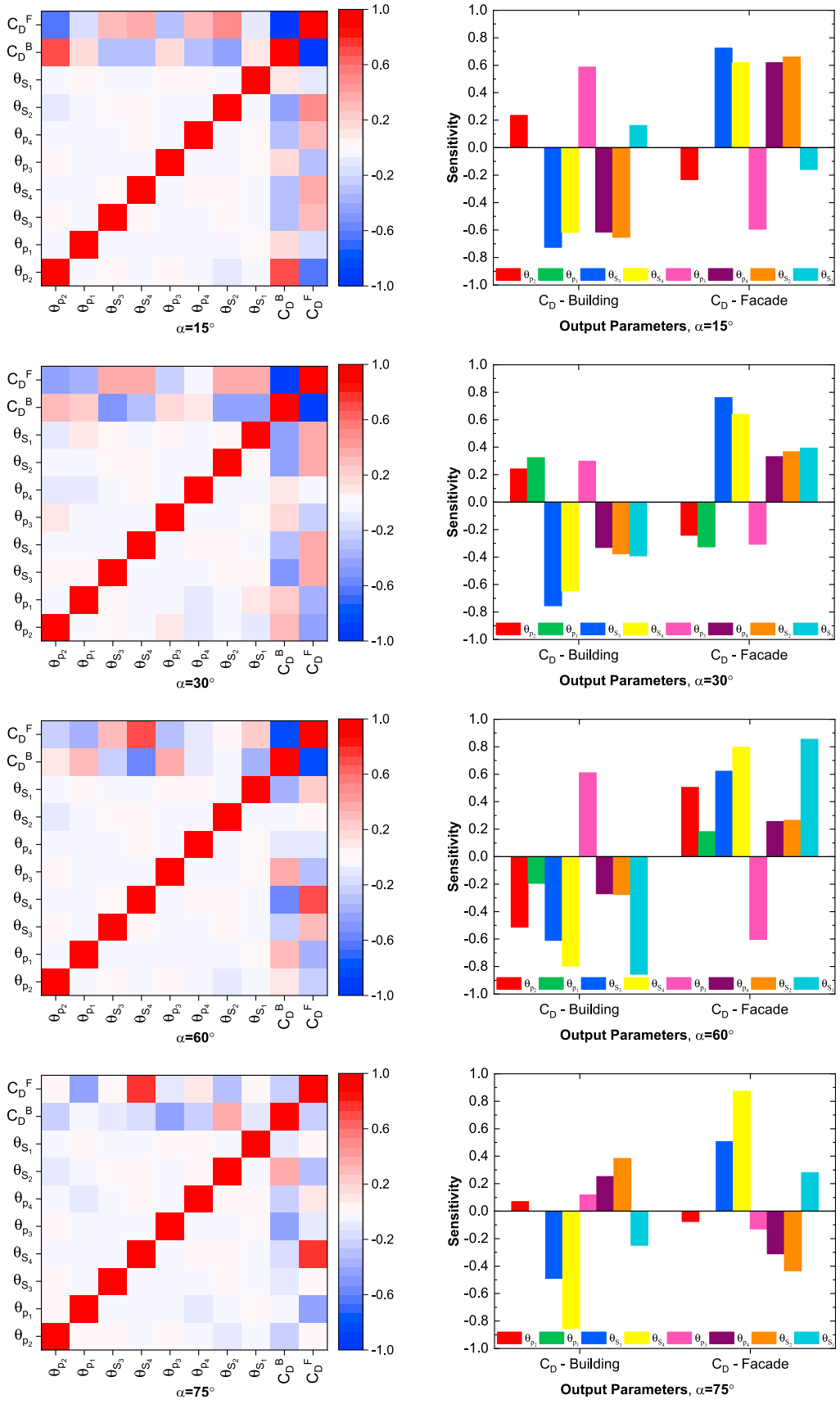

Fig. A3. Correlation map and sensitivity analysis for design variables and response or output parameters.

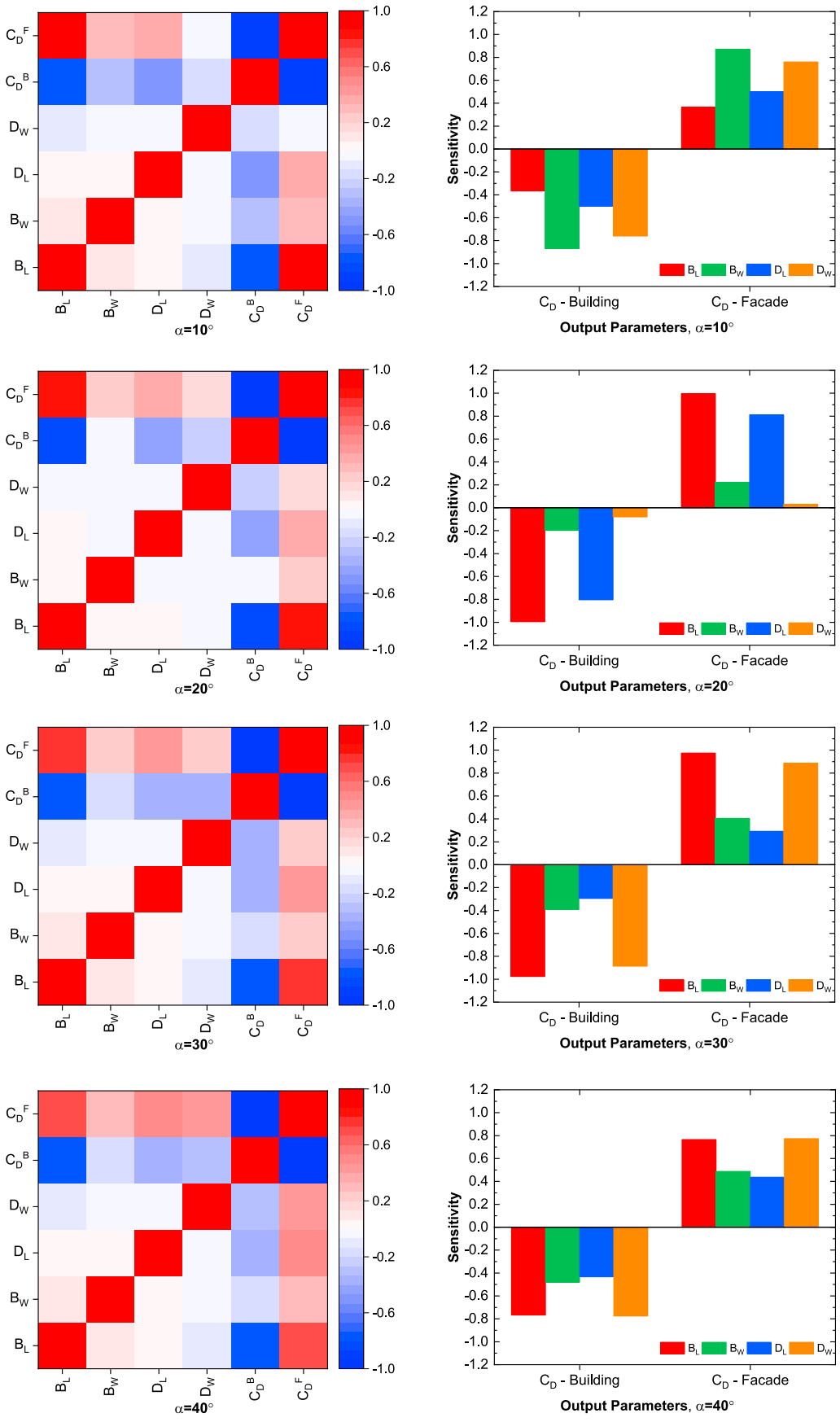

Fig. A4. Correlation map and sensitivity analysis for the elliptical double façade.

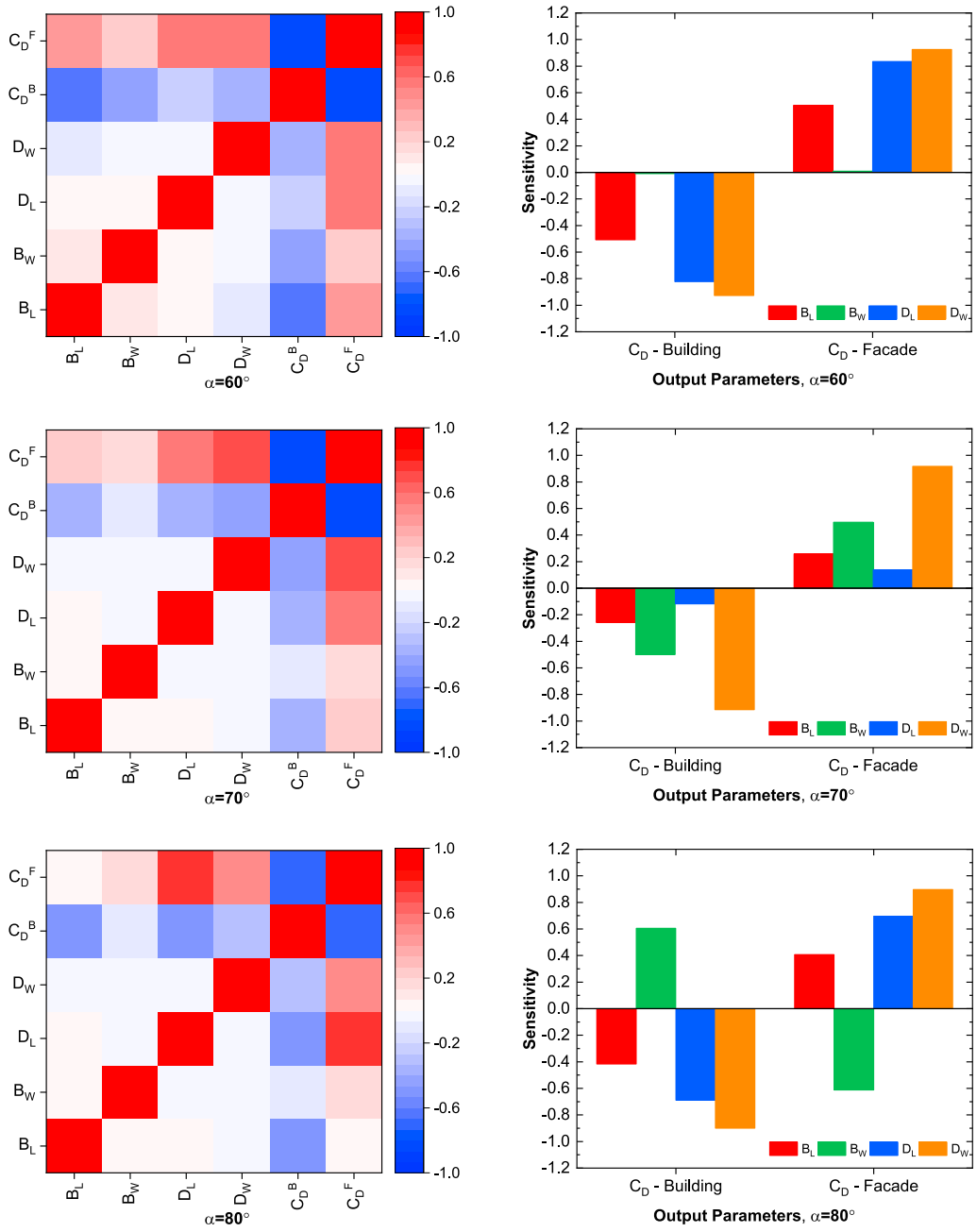

Fig. A4. (*continued*).

References

Abdelaziz, K, Alipour, A., Hobeck, J., 2021 May. A smart façade system controller for optimized wind-induced vibration mitigation in tall buildings. J. Wind Eng. Ind. Aerod. 212, 104601.

Agathokleous, R.A., Kalogirou, S.A., 2016. Double skin facades (DSF) and building integrated photovoltaics (BIPV): a review of configurations and heat transfer characteristics. Renew. Energy 89, 743–756.

Al-Share, F., 2020. No Title.

Antony, J., 2014. Design of Experiments for Engineers and Scientists. Elsevier.

Arora, J.S., 2004a. Introduction to Optimum Design. Academic Press.

Arora, J.S., 2004b. Introduction to Optimum Design. Elsevier.

Attia, S., Bilir, S., Safy, T., Struck, C., Loonen, R., Goia, F., 2018. Current trends and future challenges in the performance assessment of adaptive façade systems. Energy Build. 179, 165–182.

Baker, C.J., 1979. The laminar horseshoe vortex. J. Fluid Mech. 95, 347–367.

Barbosa, S., Ip, K., 2014. Perspectives of double skin façades for naturally ventilated buildings: a review. Renew. Sustain. Energy Rev. 40, 1019–1029.

Baş, D., Boyacı, I.H., 2007. Modeling and optimization I: usability of response surface methodology. J. Food Eng. 78, 836–845.

Başaran, T., İnan, T., 2016. Experimental investigation of the pressure loss through a double skin facade by using perforated plates. Energy Build. 133, 628–639.

Bernardini, E., Spence, S.M., Wei, D., Kareem, A., 2015. Aerodynamic shape optimization of civil structures: a CFD-enabled Kriging-based approach. J. Wind Eng. Ind. Aerod. 144, 154–164.

Box, G.E., Wilson, K.B., 1951. On the experimental attainment of optimum conditions. J. R. Stat. Soc. Ser. b 13, 1–38.

Da Silva, F.M., Gomes, M.G., 2008. Gap inner pressures in multi-storey double skin facades. Energy Build. 40, 1553–1559.

Daemei, A.B., Eghbali, S.R., 2019. Study on aerodynamic shape optimization of tall buildings using architectural modifications in order to reduce wake region. Wind Struct. 29, 139–147.

Deb, K., Agrawal, S., Pratap, A., Meyarivan, T., 2000. A fast elitist non-dominated sorting genetic algorithm for multi-objective optimization: NSGA-II. In: International Conference on Parallel Problem Solving from Nature, pp. 849–858.

Deb, K., Pratap, A., Agarwal, S., Meyarivan, T.A.M.T., 2002. A fast and elitist multiobjective genetic algorithm: NSGA-II. In: IEEE Transactions on Evolutionary Computation, pp. 182–197.

Domjan, S., Petek, L., Arkar, C., Medved, S., 2020. Experimental study on energy efficiency of multi-functional BIPV glazed façade structure during heating season. Energies 3, 2772.

Elshaer, A., Bitsuamlak, G., El Damatty, A., 2015. Aerodynamic shape optimization for corners of tall buildings using CFD. In: 14th International Conference on Wind Engineering, Porto Alegre, Brazil.
Farrokhzad, M., Nayebi Fahandari, Z., 2014. Double skin glass façade and its effect on saving energy TT -. Int. J. Archit. Eng. Urban Plan. 24, 65–74.
Gerhardt, H.J., Janser, F., 1994. Wind loads on wind permeable facades. J. Wind Eng. Ind. Aerod. 53, 37–48.
Gerhardt, H.J., Kramer, C., 1983. Wind loads on wind-permeable building facades. J. Wind Eng. Ind. Aerod. 11, 1–20.
GhaffarianHoseini, Ali, GhaffarianHoseini, Amirhosein, Berardi, U., Tookey, J., Li, D.H.W., Kariminia, S., 2016. Exploring the advantages and challenges of double-skin façades (DSFs). Renew. Sustain. Energy Rev. 60, 1052–1065.
Hassanli, S., Hu, G., Fletcher, D.F., Kwok, K.C.S., 2018a. Potential application of double skin façade incorporating aerodynamic modifications for wind energy harvesting. J. Wind Eng. Ind. Aerod. 174, 269–280.
Hassanli, S., Hu, G., Kwok, K.C.S., Fletcher, D.F., 2017. Utilizing cavity flow within double skin façade for wind energy harvesting in buildings. J. Wind Eng. Ind. Aerod. 167, 114–127.
Hassanli, S., Kwok, K.C.S., Zhao, M., 2018b. Performance assessment of a special double skin façade system for wind energy harvesting and a case study. J. Wind Eng. Ind. Aerod. 175, 292–304.
Heddleson, C.F., Brown, D.L., Cliffe, R.T., 1957. Summary of Drag Coefficients of Various Shaped Cylinders.
Hou, F., Jafari, M., 2020. Investigation approaches to quantify wind-induced load and response of tall buildings: a review. Sustain. Cities Soc. 62, 102376. https://doi.org/10.1016/j.scs.2020.102376.
Hou, F., Sarkar, P.P., 2018. A time-domain method for predicting wind-induced buffeting response of tall buildings. J. Wind Eng. Ind. Aerod. 182, 61–71.
Hu, G., Hassanli, S., Kwok, K.C.S., Tse, K.T., 2017. Wind-induced responses of a tall building with a double-skin façade system. J. Wind Eng. Ind. Aerod. 168, 91–100.
Hu, G., Song, J., Hassanli, S., Ong, R., Kwok, K.C.S., 2019. The effects of a double-skin façade on the cladding pressure around a tall building. J. Wind Eng. Ind. Aerod. 191, 239–251.
Jafari, M., Sankar, P., Alipour, A., 2019. A numerical simulation method in time domain to study wind-induced excitation of traffic signal structures and its mitigation. J. Wind Eng. Ind. Aerod. 193, 103965. pp.1–18.
Jafari, M., Alipour, A., 2020. Methodologies to mitigate wind-induced vibration of tall buildings: a state-of-the-art review. J. Build. Eng. 101582.
Jiru, T.E., Taob, Y.X., Haghighat, F., 2011. Airflow and heat transfer in double skin facades. Energy Build. 43, 2760–2766.
Kalitzin, G., Medic, G., Iaccarino, G., Durbin, P., 2005. Near-wall behavior of RANS turbulence models and implications for wall functions. J. Comput. Phys. 204, 265–291.
Kenway, G.K., Martins, J.R., 2016. Multipoint aerodynamic shape optimization investigations of the common research model wing. AIAA J. 54, 113–128.
Kwok, K.C., Samali, B., Hu, G., Tse, K.T., 2014. Wind-induced response reduction of a tall building with an innovative façade system. In: 23rd Australasian Conference on the Mechanics of Structures and Materials (ACMSM23), pp. 993–998.
Lou, W., Huang, M., Zhang, M., Lin, N., 2012. Experimental and zonal modeling for wind pressures on double-skin facades of a tall building. Energy Build. 54, 179–191.
Lou, W., Zhang, M., Shen, G., 2009. Wind tunnel test study on mean wind pressure distribution for double-skin facade. J. Build. Struct. 120–125.
Lou, W.J., Li, H., Wei, K.Z., Chen, Y., Li, H.L., 2008. Wind tunnel test study on wind pressure distribution on double-skin facades of high-rise buildings with typical shapes. J. Harbin Inst. Technol. 40, 296–301.
Manshadi, M.D., Aghajanian, S., 2018. Computational aerodynamic optimization of wing-design concept at supersonic conditions by means of the response surface method. J. Brazilian Soc. Mech. Sci. Eng. 40.
Micheli, L., Alipour, A., Laflamme, S., 2020a. Multiple-surrogate models for probabilistic performance assessment of wind-excited tall buildings under uncertainties. ASCE-ASME Journal of Risk and Uncertainty in Engineering Systems, Part A: Civ. Eng. 6 (4), 1–12, 04020042.
Micheli, L., Hong, J., Laflamme, S., Alipour, A., 2020b. Surrogate models for high performance control systems in wind-excited tall buildings. Journal of Applied Soft Computing 90, 1–15, 106133.
Micheli, L., Cao, L., Laflamme, S., Alipour, A., 2020c. Life cycle cost evaluation strategy for high performance control systems under uncertainties. ASCE J. Eng. Mech. 146 (2), 1–15, 04019134.
Micheli, L., Alipour, A., Laflamme, S., Sarkar, P., 2019. Performance-based design with life-cycle cost assessment for damping systems integrated in wind excited tall buildings. J. Eng. Struc. 195, 438–451.
Micheli, L., Alipour, A., Laflamme, S., 2021. Life-cycle cost optimization of wind-excited tall buildings using surrogate models. Struct. Des. Tall Special Build. https://doi.org/10.1002/tal.1840.
Micheli, L., Micheli, L., Cao, L., Gong, Y., Cancelli, A., Laflamme, S., Alipour, A., 2017. Probabilistic performance-based design for high performance control systems. Active and Passive Smart Structures and Integrated Systems 10164, 101642I, 2017.
Montazeri, H., Blocken, B., Janssen, W.D., van Hooff, T., 2013. CFD evaluation of new second-skin facade concept for wind comfort on building balconies: case study for the Park Tower in Antwerp. Build. Environ. 68, 179–192.
Moon, K.S., 2011. Structural design of double skin facades as damping devices for tall buildings. Procedia Eng 14, 1351–1358.
Moon, K.S., 2009. Tall building motion control using double skin façades. J. Architect. Eng. 15, 84–90.
Myers, R.H., Montgomery, D.C., Anderson-Cook, C.M., 2016. Response Surface Methodology: Process and Product Optimization Using Designed Experiments. John Wiley & Sons.
Parashar, S., Bloebaum, C., 2006. Multi-objective genetic algorithm concurrent subspace optimization (MOGACSSO) for multidisciplinary design. In: 47th AIAA/ASME/ASCE/AHS/ASC Structures, Structural Dynamics, and Materials Conference, p. 2047.
Peterka, J.A., Meroney, R.N., Kothari, K.M., 1985. Wind flow patterns about buildings. J. Wind Eng. Ind. Aerod. 21, 21–38.
Pomaranzi, G., Daniotti, N., Schito, P., Rosa, L., Zasso, A., 2020. Experimental assessment of the effects of a porous double skin façade system on cladding loads. J. Wind Eng. Ind. Aerod. 196, 104019.
Pomponi, F., Piroozfar, P.A.E., Southall, R., Ashton, P., Farr, E.R.P., 2016. Energy performance of double-skin façades in temperate climates: a systematic review and meta-analysis. Renew. Sustain. Energy Rev. 54, 1525–1536.
Potangaroa, R., Aynsley, R., 2003. Pressure distributions behind double facades. The implications for natural ventilation. In: Proceedings of the 11th International Conference on Wind Engineering, pp. 713–720.
Samali, B., Azad, A., Ngo, T., 2014. Control of wind-induced motion of mid-rise buildings using smart facade systems. In: Sixth World Conference on Structural Control and Monitoring: Proceedings of the 6th Edition of the World Conference of the International Association for Structural Control and Monitoring (IACSM), pp. 2856–2863.
Sattar, A.M.A., Elhakeem, M., Gerges, B.N., Gharabaghi, B., Gultepe, I., 2018. Wind-induced air-flow patterns in an urban setting: observations and numerical modeling. Pure Appl. Geophys. 175, 3051–3068.
Song, C.C.S., He, J., 1993. Computation of wind flow around a tall building and the large-scale vortex structure. J. Wind Eng. Ind. Aerod. 46–47, 219–228.
Stec, W.J., Van Paassen, A.H.C., Maziarz, A., 2005. Modelling the double skin façade with plants. Energy Build. 37, 419–427.
Thompson, J., Walton, S., Hassan, O., Rolland, S., Sienz, J., 2017. The use of CFD and multi-objective optimisation techniques to customise an industrial pre-mixer. Struct. Multidiscip. Optim. 55, 2339–2351.
Wardlaw, R.L., Moss, G.F., 1970. A standard tall building model for the comparison of simulated natural winds in wind tunnels. CAARC, CC 662m Tech 25.
Yang, S., Cannavale, A., Prasad, D., Sproul, A., Fiorito, F., 2019. Numerical simulation study of BIPV/T double-skin facade for various climate zones in Australia: effects on indoor thermal comfort. Build. Simul. 12, 51–67.